UNIVERSITÀ DEGLI STUDI DI PALERMO
SCUOLA POLITECNICA

CORSO DI LAUREA MAGISTRALE IN INGEGNERIA ELETTRONICA

Impedance measurements and simulations for the LHC and HL-LHC injection protection collimator

University supervisor:

Prof. Enrico CALANDRA

CERN supervisors:

Dr. Benoît SALVANT

Dr. Nicolò BIANCACCI

Author:

Edoardo BONANNO

September 20, 2016

ACADEMIC YEAR 2015 - 2016

Acknowledgements

I would like to express my deepest gratitude to Dr. Benoît Salvant, my CERN supervisor, for giving me the wonderful opportunity to work and write my thesis at CERN. I had the chance to benefit from his wide preparation and his teachings, always accompanied by his nice words of encouragement and good mood.

Another CERN colleague and friend I want to mention is Dr. Nicolò Biancacci. Despite he was not my supervisor and his large amount of work, he always offered me his time, his patience and his priceless help from the very start of my internship until the end of the thesis. My best wishes to him and his family.

A thankful acknowledgement to the Impedance Team, the whole HSC section and the other colleagues I met during my internship: all of them let me feel welcomed and at ease since the beginning.

Moving to the Italian side, I would also like to acknowledge my University Supervisor Prof. Enrico Calandra, who followed and encouraged me with trust and helpfulness during this experience.

And last but not least, my warmest gratitude goes to my parents, my family and my closest friends: their support and enthusiasm (especially when I was abroad studying or working) made me stronger and confident. A special mention for Totò and Franca Vanadia, Lucia and Maria Bonanno… they know why.

Contents

Chapter 1

Introduction

1.1 Objectives

This thesis focuses on the study and the data analysis of the *Injection Protection Collimator* (also *Injection Protection Target Dump* or TDI), one of the *Large Hadron Collider* (LHC) collimators at CERN, in Geneva. The last chapters also deal with the *Segmented TDI* (TDIS), the TDI upgrade for *High Luminosity-LHC* (HL-LHC).
In this chapter CERN will be briefly presented, and the LHC will be introduced. TDI and TDIS will be discussed later, after a chapter dedicated to particle accelerator physics, which we will need to better understand the key role of some parameters to obtain good device performances.

1.2 CERN

The acronym CERN represents the French words *Conseil Européen pour la Recherche Nucléaire* (European Council for Nuclear Research), which was held at the time of its foundation. It was later adopted to refer at the institution itself, that is now commonly described as the *European Organization for Nuclear Research*.
The CERN convention was signed in 1953 by the 12 founding states: Belgium, Denmark, France, the Federal Republic of Germany, Greece, Italy, the Netherlands, Norway, Sweden, Switzerland, the United Kingdom and Yugoslavia (which later left), and entered into force on 29 September 1954. The organization was subsequently joined by Austria, Spain, Portugal, Finland, Poland, Czech Republic, Slovak Republic, Hungary, Bulgaria, Israel and Romania. Today CERN has 22 member states plus other Associate members.

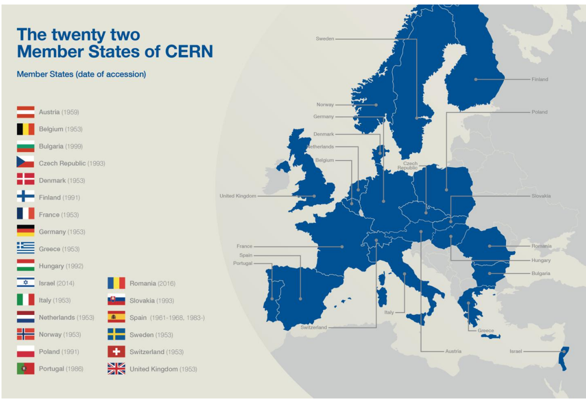

Figure 1.1: The 22 CERN member states, courtesy of CERN.

In Figure 1.1 the 22 member states are depicted. Furthermore, over 600 institutes and universities around the world use CERN's facilities. Funding agencies from both member and non-member states are responsible for the financing, construction and operation of the experiments on which they collaborate.

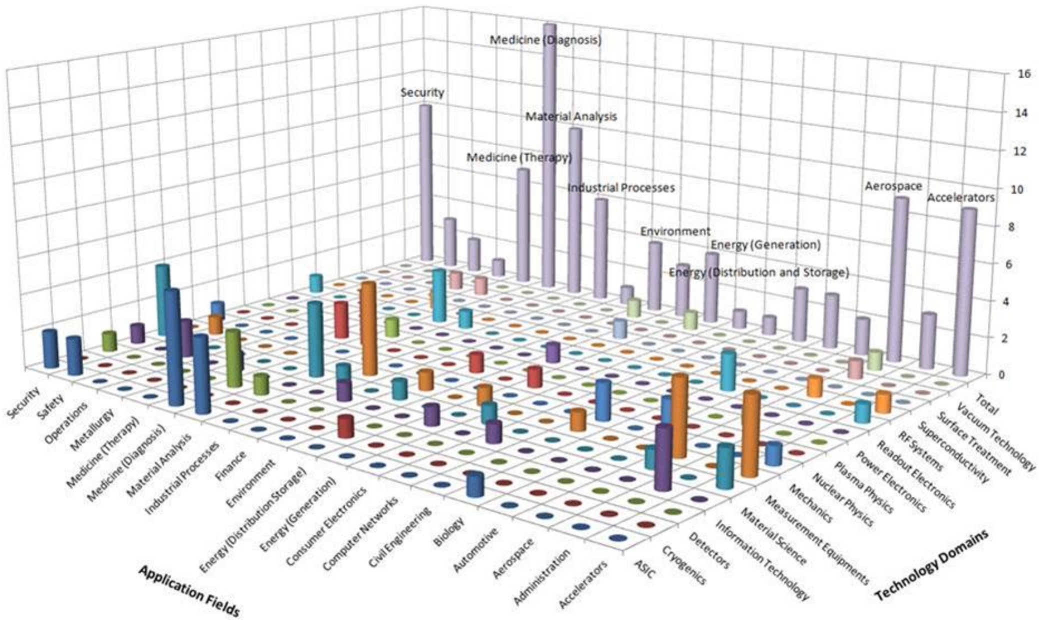

Figure 1.2: Impact of CERN technologies in different fields [1].

CERN has more than 2500 employees. Most of their efforts are focused to build particle accelerators, ensure their smooth operation, analyse and interpret data from the related experiments. Some 12000 visiting scientists from over 70 countries and with 120 different nationalities come to CERN for their researches.

CERN publications and results are available for the whole scientific community and the cutting-edge achievements in particle accelerators, detectors and computing find applications in several fields, especially in the medical one: Figure 1.2 .

The overall CERN goals are: pushing forward the frontiers of knowledge, develop new technologies and detectors, train the scientists and the engineers of tomorrow, unite people from different countries and cultures.

1.2.1 The accelerator complex and the LHC

The accelerator complex at CERN is a succession of machines that accelerate particles to increasingly higher energies. Each machine boosts the energy of a beam of particles, before injecting the beam into the next machine in the sequence (Figure 1.3). However, most of these accelerators are also directly involved in experiments at (relatively) low energies. The last element of the accelerators succession is the *Large Hadron Collider* (LHC), where beams are accelerated up to the record energy of 6.5 TeV per beam.
The proton source is a simple bottle of hydrogen gas, from which protons are yielded. The first element of the accelerator chain is *Linac 2* (Linac stands for *linear accelerator*), that accelerates the protons to the energy of 50 MeV. Afterwards, the beam is injected into the *Proton Synchrotron Booster* (PSB), followed by the *Proton Synchrotron* (PS), the *Super Proton Synchrotron* (SPS) and the LHC.

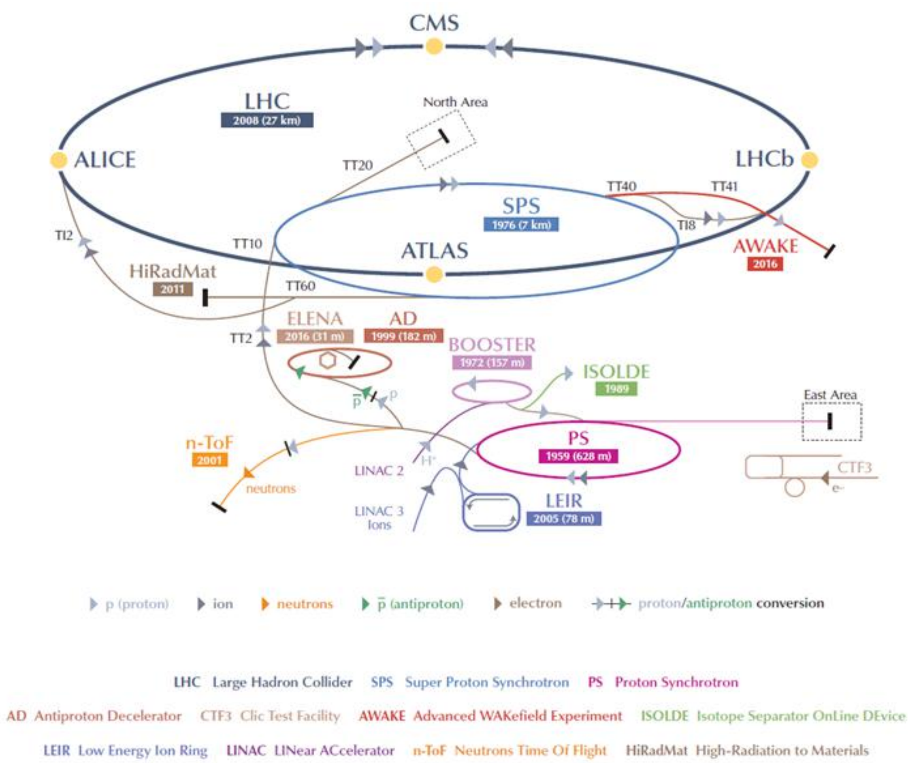

Figure 1.3: The accelerator complex, courtesy of CERN.

The LHC is the world's largest and most powerful particle accelerator. It consists of a 27 km ring of superconducting magnets with a number of different structures to boost the energy of the particles along the way and to ensure beams stability and quality.

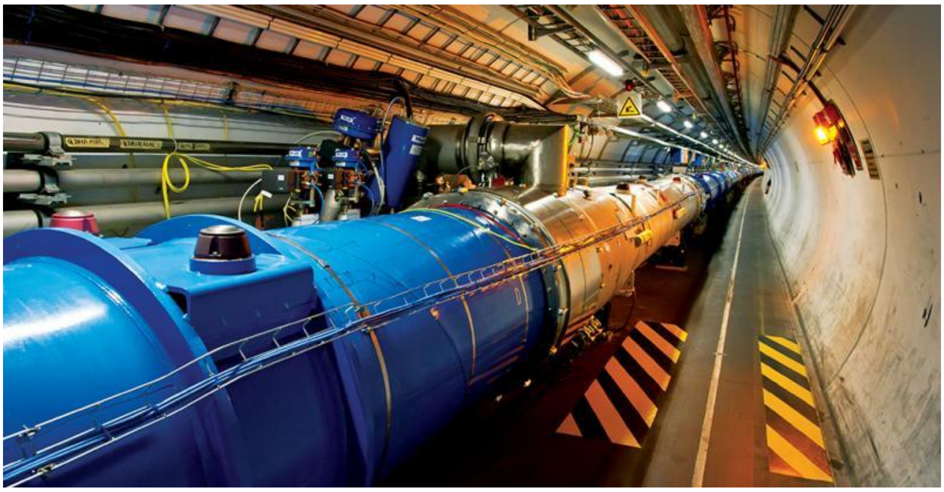

Figure 1.4: The LHC tunnel, courtesy of CERN.

The LHC has two beam pipes, kept at ultra-high vacuum: in one of them a beam circulates clockwise while the beam in the other pipe circulates anticlockwise. Thousands of super-cooled magnets of different types and sizes are used to direct the beams along the way. In the last stage, the protons reach their maximum energy of 6.5 TeV, hence travelling close to the speed of light, and are eventually brought into collision inside four detectors: ALICE, ATLAS, CMS and LHCb. The total energy at the collision point is therefore 13 TeV.
The LHC is not designed to accelerate only protons. Lead ions coming from a source of vaporized lead enter *Linac 3*. They are then accelerated in the *Low Energy Ion Ring* (LEIR) to be injected in the PS. From the PS they follow the same path of the protons to reach the maximum energy in the LHC.

Chapter 2

Concepts of particles accelerators and beams physics

In this chapter some parameters and variables will be introduced in order to better understand simulations and results which will be presented in the following.
Since there is a wide amount of literature on this topic, here the goal is not to give a complete prospective on it, rather to provide some basic notions, linked to the reference, to allow further and deeper analysis.

2.1 Luminosity

Collisions between particles have a key role in CERN studies and experiments. Thus, it is immediately obvious the interest in maximizing the amount of collisions in a collider, such as the LHC.
LHC beams are not made of a continuous stream of particles: they can be seen as a train of *bunches*. We can imagine the LHC circumference, on the nominal trajectory, as a continuous series of *buckets*, and each one of them can be filled with a bunch. Nowadays, when in full regime, the bunches per beam are 2808. Each of them is about 7.55 cm (bunchlength root mean square) and is made of 115 billions particles. Pilots bunches host a number of particles lower by orders of magnitudes compared to the nominal ones, and they are used to calibrate the machine. The bunch spacing is about 25 ns, that corresponds to one filled bucket every ten. The amount of buckets in the machine is 35640, allowing more than 2808 bunches for the given spacing but a lower number is used to ensure collisions and for restrictions on the kicker. More parameters can be found in the LHC design report [2]. Our studies in the

following chapters, unless specified, will be single-bunch studies.

As it can be expected, the number of collisions per second dR/dt, called *events*, depends on the number of particles per bunch (N_b), on the number of bunches (n_b), on the geometrical properties of the bunches ($\sigma_x, \sigma_y, \sigma_b$) and on the revolution frequency in the accelerator (f_0). The main parameter related to the number of events is called *Luminosity* $\mathscr{L}$, that is a function of the variables just mentioned:

$$\mathscr{L} = \frac{N_b^2 n_b f_0}{4\pi\sigma_x\sigma_y}. \tag{2.1}$$

The relation between the number of interactions per second dR/dt and the Luminosity is given by the (2.2), where σ_p is the event's cross-section.

$$\frac{dR}{dt} = \mathscr{L}\sigma_p. \tag{2.2}$$

It is important to mention that in (2.1) we are neglecting some other effects that reduce the Luminosity (for instance, crossing angle and collision offset).

2.2 Wakes and impedances

A charged particle when travelling through an accelerator will interact with the accelerator's structure itself, irradiating a field that will affect the following particles in the same bunch and in the following ones.

These beam-induced fields are called *wakefields* and, as a first approximation, we can consider them as superimposed to the external fields given by dipols, quadrupoles, RF cavities, etc.. Dipoles are responsible for the beam curvature, in order to keep it on the accelerator's orbit. Quadrupoles take care of focusing and defocusing and RF cavities of acceleration. The approximation holds since the ones we called external fields are considerably larger than the wakefileds. Furthermore, quadrupoles and dipoles variations are also much slower than wakefields' ones.

Analysis and determinations of wakefields and their frequency equivalent, the *beam coupling impedance*, is accomplished with the aid of theoretical and numerical calculations, measurements and simulations, depending on the structure's complexity and typology. These studies have a high importance since the early stages of the machine's design, aiming to understand and foresee the beam's behaviour. Wakefields can, in the worst cases, lead to beam's instabilities and, as a direct consequence, beam degradations and loss.

The impedance and the wakefields' impact can be analyzed using them as an input for beam's dynamics numerical codes (such as HEADTAIL [3]).

The most common approach, adopted for instance in [4] and [5], to define wakefields and beam coupling impedance is to consider a source charge q_S and a test one q_T, respectively at coordinates (x_S, y_S, z_S) and (x_T, y_T, z_T). Supposing that they move at the same speed v = βc, where β is the relativistic velocity factor, they will maintain a constant distance between each other (approximation which is called *rigid motion*). Thus we can calculate the momentum variation $\Delta\mathbf{p}$, that will depend on both source and test charge positions:

$$\Delta\mathbf{p} = \int_{-\infty}^{+\infty} \mathbf{F}(x_S, y_S, z_S, x_T, y_T, z_T)\, dt. \tag{2.3}$$

The force $\mathbf{F}$ considered is the Lorentz force (2.4):

$$\mathbf{F} = q(\mathbf{E} + \mathbf{v} \times \mathbf{B}). \tag{2.4}$$

The *wake functions* (wakefields, in the following), are defined as

$$W(x_S, y_S, z_S, x_T, y_T, z_T)\left[\frac{V}{C}\right] = -\frac{v}{q_S q_T}\Delta p. \tag{2.5}$$

The problem can be decomposed on transverse plane and longitudinal axis, using a generic cylindrical coordinate system and starting from electric and magnetic fields: $\mathbf{E} = E_l\ \hat{\mathbf{z}} + E_t\ \hat{\mathbf{t}}$ and $\mathbf{B} = B_l\ \hat{\mathbf{z}} + B_t\ \hat{\mathbf{t}}$, respectively. Since $\mathbf{v} = v\ \hat{\mathbf{z}}$, the magnetic field does not give any contribution to the longitudinal component of the force and, therefore, neither to the momentum, nor to the wakefields. Thus, we obtain:

$$W_{l,t}(x_S, y_S, z_S, x_T, y_T, z_T) = -\frac{v}{q_S q_T}\Delta p_{l,t}. \tag{2.6}$$

Where the subscripts l and t stand for longitudinal and transverse. Δp_l and Δp_t are expressed in (2.7) and (2.8), respectively.

$$\Delta p_l = \int_{-\infty}^{+\infty} q_T\ E_l\ dt, \tag{2.7}$$

$$\Delta p_t = \int_{-\infty}^{+\infty} q_T E_t + q_T c\beta B_t\ dt. \tag{2.8}$$

W_l can be developed with a Taylor expansion in the source and test charges offsets. Referring to the longitudinal wakefield, usually one is talking about the zero term of this expansion, that

is also independent from the offsets. In the case of axisymmetric structures (i.e. symmetric with respect to an axis of rotation, in this case the longitudinal one) and null offsets (i.e. $x_S = y_S = x_T = y_T = 0$) W_l will exactly coincide with the zero term of its expansion.
As for the transverse, W_t can also be expanded in a series of powers:

$$
\begin{aligned}
W_{tx}(x_S, z_S, x_T, z_T) &\approx W_{tx}(0, z_S, 0, z_T) + \\
&+ \nabla_t W_{tx}(x_S, z_S, x_T, z_T)|_{x_T=0}\, x_S + \\
&+ \nabla_t W_{tx}(x_S, z_S, x_T, z_T)|_{x_S=0}\, x_T, \\
W_{ty}(y_S, z_S, y_T, z_T) &\approx W_{ty}(0, z_S, 0, z_T) + \\
&+ \nabla_t W_{ty}(y_S, z_S, y_T, z_T)|_{y_T=0}\, y_S + \\
&+ \nabla_t W_{ty}(y_S, z_S, y_T, z_T)|_{y_S=0}\, y_T.
\end{aligned}
\tag{2.9}
$$

With the positions (2.10) we can again write (2.9), defining respectively W_x e W_y as the approximations of W_{tx} and W_{ty} at their first order (2.11).

$$
\begin{aligned}
W_x^{cst}\left[\tfrac{V}{C}\right] &= W_{tx}(0, z_S, 0, z_T), \\
W_x^{dip}\left[\tfrac{V}{C\,m}\right] &= W_{tx}(x_S, z_S, x_T, z_T)|_{x_T=0}, \\
W_x^{quad}\left[\tfrac{V}{C\,m}\right] &= W_{tx}(x_S, z_S, x_T, z_T)|_{x_S=0}, \\
W_y^{cst}\left[\tfrac{V}{C}\right] &= W_{ty}(0, z_S, 0, z_T), \\
W_y^{dip}\left[\tfrac{V}{C\,m}\right] &= W_{ty}(y_S, z_S, y_T, z_T)|_{y_T=0}, \\
W_y^{quad}\left[\tfrac{V}{C\,m}\right] &= W_{ty}(y_S, z_S, y_T, z_T)|_{y_S=0}.
\end{aligned}
\tag{2.10}
$$

The zero term is a constant (independent from source and test's positions) which is null for axisymmetric structures. W_x^{dip} and W_x^{quad} are called *horizontal dipolar wakefield* (also *driving* instead of dipolar) and *horizontal quadrupolar wakefield* (also *detuning* instead of quadrupolar), respectively. Their vertical correspondents are defined on the y axis.

$$
\begin{aligned}
W_x &= W_x^{cst} + W_x^{dip} x_S + W_x^{quad} x_T, \\
W_y &= W_y^{cst} + W_y^{dip} y_S + W_y^{quad} y_T.
\end{aligned}
\tag{2.11}
$$

In case of axisymmetric structures and null offsets, W_x and W_y become zero as it was reasonable to expect, because there are no reasons for a direction to be preferred to the others, with the given conditions.
The *beam coupling impedance* (impedance, in the following) is defined as the Fourier transform of the wakefield:

$$
\begin{aligned}
Z_l(x_S,y_S,x_T,y_T,\omega)\ [\Omega] &= \int_{-\infty}^{+\infty} W_l(x_S,y_S,z_S,x_T,y_T,z_T)\ e^{j\omega s/v}\ \frac{ds}{v}\ \ and \\
Z_t(x_S,y_S,x_T,y_T,\omega)\ [\Omega] &= -j\int_{-\infty}^{+\infty} W_t(x_S,y_S,z_S,x_T,y_T,z_T)\ e^{j\omega s/v}\ \frac{ds}{v},
\end{aligned}
\tag{2.12}
$$

where $s = z_T - z_S$ can be used because, following the hypothesis of rigid bunch, the wakefields only depend on the distance between source and test charge, and not on their absolute position.

Following from (2.12), antitransforming the impedance we can obtain back the wakefields (2.13).

$$
\begin{aligned}
W_l(x_S,y_S,z_S,x_T,y_T,z_T) &= \frac{1}{2\pi}\int_{-\infty}^{+\infty} Z_l(x_S,y_S,x_T,y_T,\omega)\ e^{-j\omega s/v}\ d\omega, \\
W_t(x_S,y_S,z_S,x_T,y_T,z_T) &= \frac{j}{2\pi}\int_{-\infty}^{+\infty} Z_t(x_S,y_S,x_T,y_T,\omega)\ e^{-j\omega s/v}\ d\omega.
\end{aligned}
\tag{2.13}
$$

For each wakefield term we defined above we can also define the equivalent in the frequency domain:

$$
\begin{aligned}
Z_x\ [\Omega] &= Z_x^{cst} + Z_x^{dip} x_S + Z_x^{quad} x_T, \\
Z_y\ [\Omega] &= Z_y^{cst} + Z_y^{dip} y_S + Z_y^{quad} y_T.
\end{aligned}
\tag{2.14}
$$

Beam coupling impedance can also be directly defined in the frequency domain [6]. An example of solving method in the frequency domain is the *Mode Matching* [5]. We will not go into details on this point also because CST, a software that will be used in the following in order to derive wakefields and impedances (chapter 5 and chapter 6), performs calculations in the time domain.

More specifically, our interest in impedance mainly lies on the transverse impedance imaginary part and on the longitudinal impedance real part. The former gives the main contribution to the machine's *tune shift* (section 2.3) while the latter is directly related to the energy loss of the bunch, as it will be shown in the following derivation.

Starting from the longitudinal wakefield definition, we have

$$
\begin{aligned}
W_l(z_T - z_S) &= -\frac{\Delta E(z_T - z_S)}{q_S\ q_T} \ \ \text{and} \\
\Delta E(z_T - z_S) &= -W_l(z_T - z_S)\ q_T\ q_S,
\end{aligned}
\tag{2.15}
$$

where we used the rigid beam approximation to write both wakefield and energy variation as functions of the distance between test and source charge.

We will now define the bunch longitudinal charge distribution as $\lambda(z)$, which gives the number of charges per unit length normalized to the total number of charges in the bunch N_b. This normalization can be mathematically expressed in the following way:

$$\int_{-\infty}^{+\infty} \lambda(z)\, dz = 1. \tag{2.16}$$

The amount of electrical charge in a bunch slice of thickness dz' at coordinate z' is therefore $\lambda(z')\, N_b\, e\, dz'$, where e is the particle charge. Replacing source and test charges in (2.15) with generic source and test slices, we obtain the following:

$$dE(z_T - z_S) = -W_l(z_T - z_S)\, \lambda(z_T)\, \lambda(z_S)\, N_b^2\, e^2\, dz_T\, dz_S. \tag{2.17}$$

where $dE(z_T - z_S)$ stands for the energetic variations given by a source slice of the bunch at z_S acting on a test slice at z_T. In order to obtain the whole bunch energetic variation we should integrate twice:

$$\Delta E = -\int_{-\infty}^{+\infty} dz_T \int_{z_T}^{+\infty} dz_S\;\; W_l(z_T - z_S)\, \lambda(z_T)\, \lambda(z_S)\, N_b^2\, e^2. \tag{2.18}$$

The source position integration starts from z_T because, at ultrarelativistic velocities, the sources that can affect a test slice are only the ones preceding it. We can than use the property of the convolution to replace the convolution integral between W_l and $\lambda(z_S)$ with the inverse Fourier transform of their Fourier transforms product:

$$\Delta E = -\int_{-\infty}^{+\infty} dz_T \int_{-\infty}^{+\infty} \frac{d\omega}{2\pi}\;\; Z_l(\omega)\, \Lambda(\omega)\, e^{-j\omega z_T/v} \lambda(z_T)\, N_b^2\, e^2, \tag{2.19}$$

where $\Lambda(\omega)$ is the Fourier transform of $\lambda(z)$. Using the other integration in dz_T, we can also transform the remaining $\lambda(z_T)$ into $\Lambda^*(\omega)$:

$$\begin{aligned}
\Delta E &= -\frac{N_b^2\, e^2}{2\pi} \int_{-\infty}^{+\infty} d\omega\;\; Z_l(\omega)\, \Lambda(\omega) \left[\int_{-\infty}^{+\infty} dz_T\;\; e^{j\omega z_T/v} \lambda(z_T) \right]^* = \\
&= -\frac{N_b^2\, e^2}{2\pi} \int_{-\infty}^{+\infty} d\omega\;\; Z_l(\omega)\, \Lambda^*(\omega)\, \Lambda(\omega) = \\
&= -\frac{N_b^2\, e^2}{2\pi} \int_{-\infty}^{+\infty} d\omega\;\; Z_l(\omega)\, |\Lambda(\omega)|^2.
\end{aligned} \tag{2.20}$$

Since the wakefields are real, it can be proved that:

$$
\begin{aligned}
Z_l^*(\omega) &= Z_l(-\omega) \text{ and} \\
Z_t^*(\omega) &= -Z_t(-\omega).
\end{aligned}
\tag{2.21}
$$

The former implies that the longitudinal impedance imaginary part is odd. Because of the real nature of $\lambda(z)$, $|\Lambda(\omega)|^2$ is an even function and the product $\mathrm{Im}[Z_l(\omega)]\ |\Lambda(\omega)|^2$ is necessarily odd. Since the contribution of an odd function in an integral with symmetric integration limits is null, the longitudinal impedance real part is the only impedance component left for the evaluation of the losses caused by the wakefields.

$$
\Delta E = -\frac{N_b^2\, e^2}{2\pi} \int_{-\infty}^{+\infty} d\omega\ \ \mathrm{Re}[Z_l(\omega)]\ |\Lambda(\omega)|^2. \tag{2.22}
$$

The fact that $\mathrm{Re}[Z_l(\omega)]$ is the only relevant part of $Z_l(\omega)$ to evaluate the energy loss can also be deduced from the final step of (2.20): since ΔE is real and all the other terms are real, the longitudinal impedance imaginary part must necessarily cross out in the integration and can be excluded from the integration in the first place.

2.3 Coherent tune shift and phase shift

Betatron oscillations, firstly defined for the category of accelerators named *betatrons* and later adopted also for the other accelerator designs, are the particles transverse oscillations along the nominal trajectory [7, p. 19] (Figure 2.1). The betatron motion is determined by the machine's arrangement of quadrupoles, called the accelerator *lattice*.

Furthermore, particle beams have a finite dispersion of momenta around the ideal momentum p_0. A particle with momentum $p \neq p_0$ will perform betatron oscillations around a closed orbit different from the reference one. This happens because the dipoles, which are responsible for the trajectory's bending, will in fact act on each particle depending on its momentum, giving rise to different orbits for particles with different momenta.

We can define the *coherent betatron tune* Q_u as the number of bunch's center of mass transverse oscillations on the axis u per turn. u can either be the x axis or the y axis. We distinguish incoherent and coherent tune since in the former we deal with the single particle within the bunch, whereas in the latter with the center of mass. In the following we will only deal with coherent betatron tune, therefore it will be simply addressed as *tune*, unless specified.

Letting $\omega_{\beta u}$ be the angular frequency associated with the betatron oscillations along the u

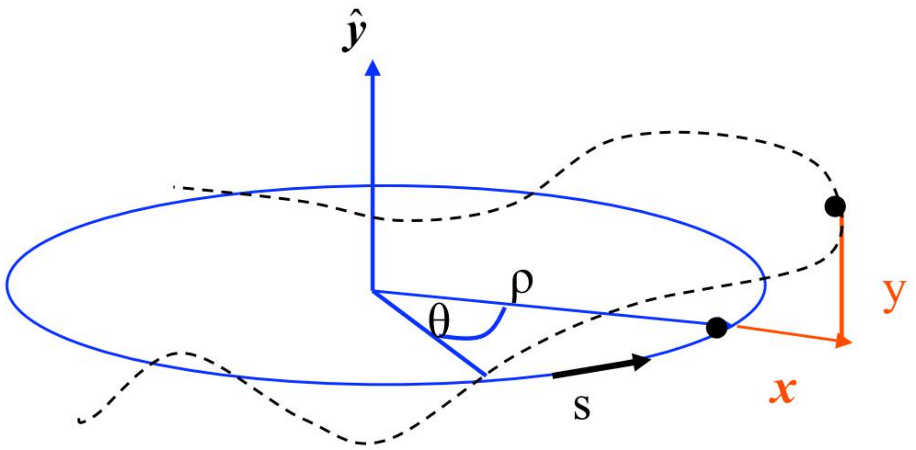

Figure 2.1: Schematization of betatron oscillations [8].

axis and ω_0 the revolution angular frequency, the tune can be expressed as:

$$\omega_{\beta u} = Q_u \omega_0. \tag{2.23}$$

To get stable off-momentum orbits, the operating tune values (working point) must be chosen to avoid resonances. For instance, a real machine necessarily have errors in the magnetic fields induced by the dipoles. These errors perturb the orbit at each turn and, for an integer tune, they would increase the transverse oscillations' amplitude. Maxima and minima would in fact be located at the same positions every turn, growing larger in amplitude. We will mainly focus on the fractional part of the tune and it must be controlled to within better than 0.001, during all machine phases.

Our work deals with the TDI and the TDIS, whose main transverse effects are on the y axis, i.e. the normal to the plane of the nominal orbit. Formulas we will provide in the following are therefore particularized to the y axis.

Using s as the coordinate along the nominal beam's orbit and y(s) as the transverse position of a particle on the y axis, the vertical equation of motion can be derived [9]:

$$\frac{d^2y}{d^2s} + K_0(s)\, y = 0. \tag{2.24}$$

Where $K_0(s)$ is called *effective focusing function* and describes the distribution of focusing strength along an ideal lattice [9]. In the (2.24) we neglected the effect given by the coupling with the *Syncrotron motion*, which can be described as the perturbations superimposed to the longitudinal motion. Periodically displaced magnets along the machine, especially quadrupoles, give alternating focusing and defocusing effects on the beam: the ones that focus on the vertical plane, defocus on the horizontal one. Thus, the lattice periodicity produces a pseudo-harmonic solution:

$$y(s) \propto \sqrt{\beta_y(s)}\, cos(\omega_{\beta y}\, s+\phi). \tag{2.25}$$

$\beta_y(s)$ is called *betatron function* and depends on the local lattice property [9]. ϕ is the betatron phase at t = 0. The harmonic term's phase advances by 2π every betatron oscillation or by 2πQ every machine revolution. Perturbing (2.24) with an external force, we can already expect a relation with the force's associated wakefield, thus with an impedance.

Equation (2.24) yields for a single particle. To attain the bunch's center of mass behaviour it is also required averaging over the N_b particles in the bunch. The detailed complete derivation is carried out in [5] and gives an alternative and practical way to compute the tune from a generic impedance, under some approximations such as the *rigid bunch*. In the formal approach developed, for instance, in [10] and [11], the Vlasov formalism is used to derive the frequency shift for the different bunch oscillation azimuthal and radial modes. Considering the bunch as a rigid unit corresponds in fact to the azimuthal mode 0.

Not perfectly conductive pipe and discontinuities which can be mapped to an impedance are also perturbations of the motion equation. These perturbations lead to a tune perturbation, called *tune shift* which is expressed in (2.26), for a gaussian bunch distribution and distributed impedance.

$$\Delta Q_y = -\frac{q^2 N_b}{8\pi^{3/2}\beta E_0 \sigma_t}\int_0^L \beta_y(s)\, \mathrm{Im}[Z_y^{eff}]\, ds. \tag{2.26}$$

Where E_0 is rest energy of the particle (proton, in our case) and L is the device length. Z^{eff} is called *Effective Impedance* (2.27) and it is the impedance weighted for the beam's power spectrum $\Lambda(\omega) = \mathscr{F}[\lambda(z)] = e^{-\sigma_t^2\omega^2/2}$, where $\sigma_t = \sigma_b/v$.

$$Z^{eff} = \frac{\displaystyle\int_{-\infty}^{+\infty} Z^{eff}(\omega)\, ||\Lambda(\omega)||^2\, d\omega}{\displaystyle\int_{-\infty}^{+\infty} ||\Lambda(\omega)||^2\, d\omega}. \tag{2.27}$$

As for TDI and TDIS, we will approximate $\beta_y(s)$ with a constant value for each device, obtained from MAD-X (a general purpose accelerator and lattice design program [12]) or from measurements. The distributed Z^{eff} will also be replaced with the devices ones. The approximation holds since the devices we are interested in are short compared to $\beta_y(s)$ variations along the device. Thus, (2.26) reduces to (2.28), where DUT (Device Under Test) can either be TDI or TDIS.

$$\Delta Q_y = -\frac{q^2 N_b}{8\pi^{3/2}\beta E_0 \sigma_t}\, \beta_y^{DUT}\ \mathrm{Im}[Z_y^{eff,\, DUT}]. \tag{2.28}$$

In the following chapters we will often evaluate the tune shift with benchmarked MatLab scripts, based on the same theory. The parameters used are the LHC and HL-LHC parameters at injection or flattop, depending on the case under study. The impedances fed to the scripts will be evaluated with numerical simulations (IW2D code, in section 3.3) or with electromagnetic time-domain simulations (CST, in chapter 5 and chapter 6).

To summarize: large transverse impedance imaginary part gives large tune shift, that can displace maxima and minima of the betatron oscillations, leading to resonances and, eventually, to beam instabilities and losses. However, this is not the only mechanism that can cause them.

In literature, a more generalized definition of the tune includes also an imaginary part related to instabilities rise times and depending on the real part of Z^{eff}. As rise times are not object of our interests, in the following we will deal with tune's real part and refer to it simply as tune.

As highlighted by (2.26), the tune is strongly affected by the imaginary part of the transverse impedance. Nonetheless, we will often also mention or report the real part of the longitudinal impedance because of its key role in the losses (as we have already seen in (2.22)) as in the *phase shift* evaluation [13].

Letting U be the energy provided by the RF to the protons per turn, q the proton's charge, V the RF voltage, ϕ is the longitudinal phase:

$$U = qV sin(\phi). \tag{2.29}$$

Phase shift is therefore a mis-alignment with the RF, sintom of a wrong energy amount provided to the beam or energy losses.

The longitudinal phase refers to the longitudinal position of a bunch's center of mass in the nominal orbit with respect to the RF waveform. *Phase Focusing* has a fundamental importance in any accelerator using RF, including linacs (i.e. linear particle accelerators). The RF provides the accelerating longitudinal kicks and has to be in phase with the bunch's center of mass. Unavoidably, different particles in the bunch will experience slightly different RF kicks, leading to longitudinal focusing (or defocusing) effects.

In the following chapters we will only mention the longitudinal phase shift in order to provide some ideas on the TDI performance improvements from LHC run 2015, when the device brought a considerable phase shift, to run 2016, when its phase shift was too small to be measurable.

Chapter 3

TDI - hBN

At the beginning of this chapter we will briefly introduce the *Injection Protection Collimator* (also *Injection Protection Target Dump*, TDI). In the following sections we will then describe the measurements carried out on the TDI - *hexagonal Boron Nitride* (TDI - hBN), that was installed in the LHC during run 2015: the measured sheet resistance of the coating of each block is reported at the end of section 3.2. Using these data as an input, two derivations were carried out: one evaluating the layer resistivity and the other one for its thickness, in order to consider all the possible coating degradations that could occur.

The whole range of data obtained from both the derivations was then fed to *Impedance Wake 2D* [14], a code performing numerical simulations, to attain impedances. Finally, the resulting longitudinal impedance was compared to some measurements performed on the real TDIs, immediately after they were removed from the LHC.

The study carried out and described in the present chapter allowed confirming that the responsibilities of the low performances of the TDI - hBN during LHC run 2015 mainly lied on the coating degradation, that exposed the blocks bulk material (i.e. the hBN) to the beams. The hBN blocks were in fact eventually replaced with graphite based ones during the last shutdown. The performances of the TDI with graphite based blocks, now installed in the LHC, will be object of our studies in the chapters that will follow the present one.

3.1 The TDI

The TDI is a device located in the two LHC points where the injections from the SPS take place. Its goal is to protect the LHC and its components in case of missing kicks on injected beam or asynchronous *kicker* firing on the circulating beam (Figure 3.1).

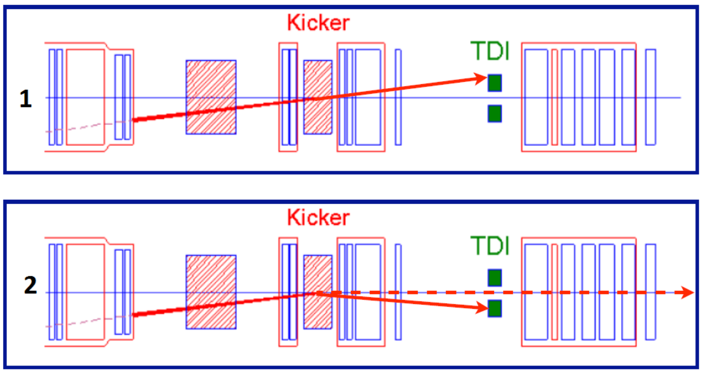

Figure 3.1: Injection schematic representation on the vertical plane. Missing kicks on injected beam (1) and asynchronous kicker firing on the circulating beam (2). Figure from [15].

The two TDIs are often referred as TDI2 and TDI8, depending on the circumference point in which they are installed: *Point 2* and *Point 8*. Alternatively, they are addressed with the name of the injected beam: *TDI - Beam 1* for the TDI2 and *TDI - Beam 2* for the TDI8.
The protection function of the TDI is mainly realized by two moving *jaws* that bring close or far from the beam in (ideally) symmetrical fashion two long series of adjacent blocks, longitudinally oriented (which means in the same direction of the beam). Thus, we can give the following definitions:

- *full gap* (or simply *gap*): the jaws aperture;
- *half gap* (*hgap*): half of the previous parameter;
- *parking position*: the condition in which the jaws are at their maximum aperture (hgap $\approx$ 55 mm) corresponding also at the machine status named *flattop*;
- *working position*: the condition in which the beam *injection* takes place (hgap = 3.8 mm).

Even if the working condition is hgap = 3.8 mm, the jaws can move closer to the beam, until hgap = 2.2 mm, before it provokes a dump.
The device must be able to let the correctly injected beams pass without alterations while it is in working position, absorbing instead the miskicked ones. Following the injection, it should retract in the parking position and become as transparent as possible to the beam, that will be soon brought to higher energy levels.
During measurements and simulations, hgap smaller than 3.8 mm have also been used in

order to have a better and more complete characterization of the device. Furthermore, as it was expected, concerning the TDI nowadays installed in the machine (the one with graphite blocks), both tune shift and phase shift were too small to be measured at the working position. In this case, only when moving the jaws closer to the beam some values were detected. They were larger than expected but at least an order of magnitude smaller than the ones for the TDI of run 2015.

3.2 Measurements on TDI - hBN blocks

During the LHC run 2015, blocks with dimensions of 15.7 cm $\times$ 5.8 cm $\times$ 5.4 cm have been used. Their structure is reported in Table 3.1: a bulk of hBN with a titanium layer coated on it.

	Material	Thickness	Resistivity
Layer 1	Titanium	5 μm	2.5 $\mu\Omega\ m$
Layer 2	hBN	54 mm	dielectric ($\varepsilon_r = 4.5$)

Table 3.1: Layers of the TDI blocks used for LHC run 2015. The layers are numerated starting from the one closest to the beam.

Figure 3.2: One of the blocks used for LHC run 2015. It was uninstalled with the others during 2015 Christmas shutdown, while the picture was taken during the measurements described in this section which were performed between March and April 2016.

The hBN is the most stable form of the ceramic compound defined as *Boron Nitride*. It has hexagonal crystal structure, similar to the graphite's one, and it is very resistant to thermal and chemical stress.

Since the blocks were inside the LHC during the operations, once they were uninstalled they showed some radioactivity. Because of this they were always stored in particular areas of CERN, dedicated to storage and handling of radioactive materials. To access this areas and be allowed to perform measurements on radioactive material, special care and authorizations are required.

During run 2015, the TDI gave significant shifts (some examples are shown in Figure 4.3 and Figure 4.4, section 4.2) and the reasons behind these shifts needed to be investigated. In regard of this, the Titanium layers quality after run 2015 was the main point of interest: the largest part of those layers was indeed deeply degraded and compromised, especially for the TDI8. Measurements on those layers were planned in order to establish and quantify how much shift was brought by their degradation.

Layers characterization required a resistivity measurement which was performed with a modified version of the four-pin method. The schematic of the setup is reported in Figure 3.3, the setup without the block in Figure 3.4 while the one with the block flipped on it is in Figure 3.5. The pictures have been taken in March and April 2016 and have been used during one of the Impedance Meetings [16].

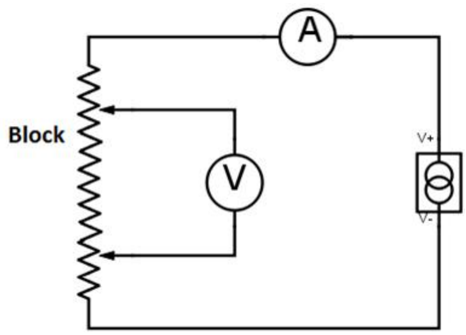

Figure 3.3: Four-pin setup schematic.

The modification of the four-pin method consisted in the use of soft contact stripes instead of pins. The soft contact stripes were pressed between the flipped block and the dielectric support and they were connected with clips to the rest of the setup. The justification of this modification is to average the local inhomogeneities along the direction perpendicular to the current, hence along the stripes. During the measurements, positions and distance between voltmetric contacts were varied in order to evaluate the level of inhomogeneity along the current direction (same as the beam's one).

The inhomogeneity level of each block was eventually mapped in the measurement's uncertainty. It is reasonable to think that these discontinuities in the layers affected the beam along its path. Moreover, they were not the same on both the beam's sides, breaking the symmetry: for a given longitudinal coordinate, the top jaw's block and the bottom jaw's one were almost never in identical conditions after they started to degrade. Eventually, the discontinuities gave contributions to the machine parameters alterations, as we will discuss later.

Figure 3.4: Four-pin setup without block.

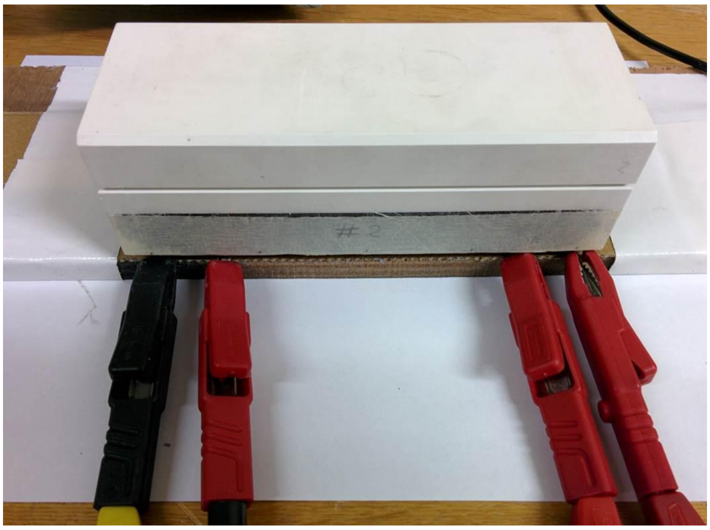

Figure 3.5: Four-pin setup with the block flipped on it.

18 voltage values per block were acquired combining 3 different current values, 3 different voltmetric contacts separation distances and 2 different orientations. However, some blocks had a coating so degraded that they resulted not measurable with the adopted instruments and setup. In the worst cases, the original Titanium layers degraded into Titanium dust, which was falling when handling the blocks.

The results in terms of coating resistivity or thickness have been calculated with MatLab

[17]. Voltage was the directly measured entity and allowed us to calculate the resistance and, provided the distance between the contacts, also a *Sheet Resistance* R_{s_i} for each voltage value.

$$R_{meas_i} = \frac{V_{meas_i}}{I_i}. \tag{3.1}$$

$$R_{s_i} = R_{meas_i} \frac{W}{L_i}. \tag{3.2}$$

In the adopted setup we always had W = 50 mm, while L was varied between 33.33 mm, 66.66 mm and 100 mm.

The four-pin method (even in its modified version) was used for the advantage offered in terms of contact resistance (R_c) extinction. This extinction was allowed by the dissociation of the amperometric and the voltmetric contacts, together with the high internal resistance of the voltmeter. Furthermore, since the measurement was performed with different values of L, the R_c was also estimated with the same principle of the *Transfer Length Method* (TLM), used in semiconductor technology to characterize ohmic contacts when the current flow is approximately two-dimensional [18].

The TLM-like calculations gave R_c small both in relative and in absolute sense, sometimes also negative, pointing to the good performance of the four-pin method. It extinguished the contact resistance to the point that, in most of the cases, it was lower than the measurement uncertainty.

The overall result of the measurement for each block are the average of the 18 values (3.3), and their standard deviations (3.4) weighted with an arbitrary confidence factor K.

$$R_s = \frac{\sum_{i=1}^{18} R_{s_i}}{18}. \tag{3.3}$$

$$std_{R_s} = K \sqrt{\frac{1}{18-1} \sum_{i=1}^{18} |R_{s_i} - R_s|^2}. \tag{3.4}$$

To obtain resistivity (ρ) or thickness (t) from R_s a supposition on the other one is needed. Mathematically, there is an infinite number of couples that satisfy the (3.5) for a given R_s.

$$\rho = R_s\, t. \tag{3.5}$$

During the study that followed the measurements, two different derivations were adopted. The former consisted in assuming the nominal titanium layer thickness (t = 5 μm) and derive the resistivity. In other words, according to this assumption the coating did not undergo any thinning, and kept its original thickness. We already knew that this derivations was only an extreme in the range of possibilities, in which we were not since many blocks showed almost no coating. As for the case of non measurable blocks (i.e. all the ones with no coating or almost no coating left), the script's algorithm was designed to return zero thickness, instead of infinite resistivity.

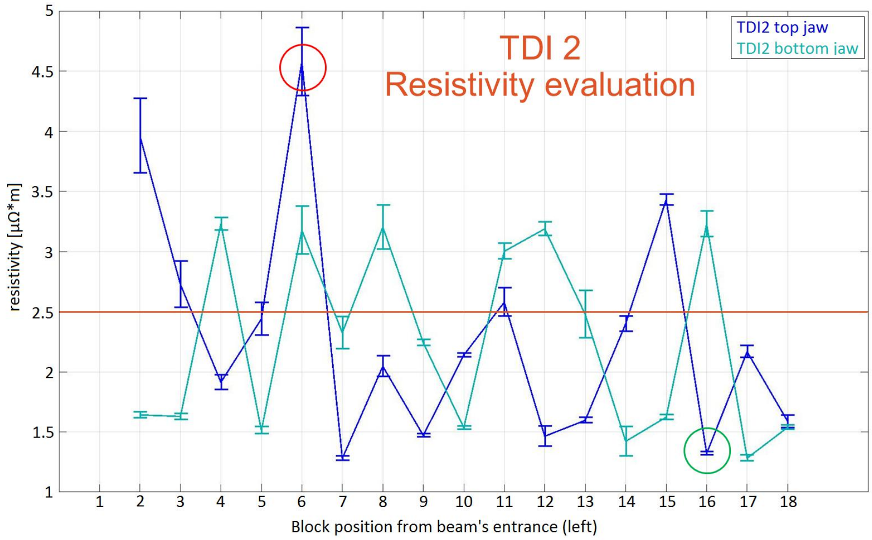

Figure 3.6: Resistivity estimations for the titanium layer in the TDI2 - hBN, assuming the nominal thickness of 5 μm (first derivation).

The first derivation for TDI2 is graphically represented in Figure 3.6. It can be observed that the resistivity value along the jaws oscillate around the expected one (solid horizontal orange line) and its average is more or less that value.

In Figure 3.8 the first derivation is depicted for both the TDIs. As it was expected, the TDI8 conditions were far worst than TDI2's, accordingly with the tune measurements performed on the LHC beam during operations (we will discuss them later in section 4.2, Figure 4.3 and Figure 4.4).

In the second derivation the expected resistivity value was assumed for all the blocks in order to calculate the thickness. The expected resistivity is not the material's nominal one: some of the imperfections induced by the machine's operations and by the imperfect coating deposition were already estimated and mapped into the expected resistivity value, higher than the nominal one. Hence, this derivation implies that the coating was uniformly deposed and that it underwent exactly the degradation that was expected during operations, while varying its thickness. Also this derivation did not represent all the blocks' status. Calculations for the blocks with the best layer conditions gave thickness larger than 5 μm. Since the coating

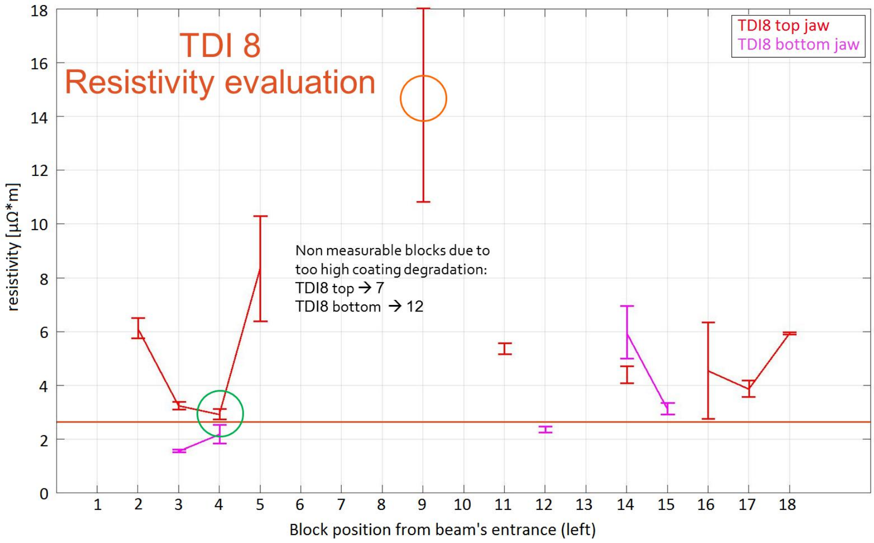

Figure 3.7: Resistivity estimations for the titanium layer in the TDI8 - hBN, assuming the nominal thickness of 5 μm (first derivation).

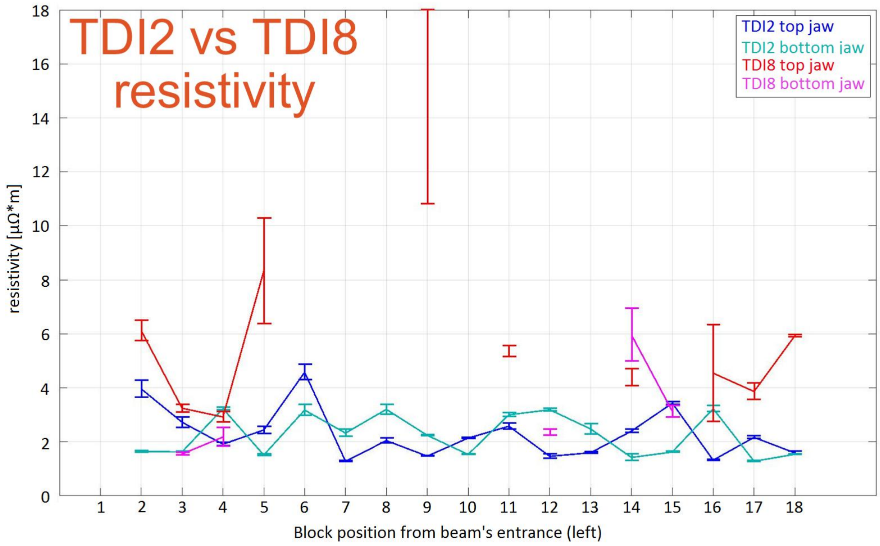

Figure 3.8: Comparison between the resistivity estimations of the titanium layer between TDI2 - hBN and TDI8 -hBN, assuming nominal thickness 5 μm (first derivation).

thickening was impossible, in this case the algorithm used the first derivation, calculating the resistivity at 5 μm thickness.

In Figure 3.9 and Figure 3.10 the second derivation is depicted for both TDI2 and TDI8, respectively. The worst conditions of the TDI8 are verifiable from the fact that a large part of the blocks gave thickness approximately null.

The colored circles in Figure 3.6, Figure 3.7, Figure 3.9 and Figure 3.10 correspond to the blocks shown in Figure 3.11 (TDI2) and Figure 3.12 (TDI8).

From visual inspection, it can be easily appreciated that the large resistivity values of the first

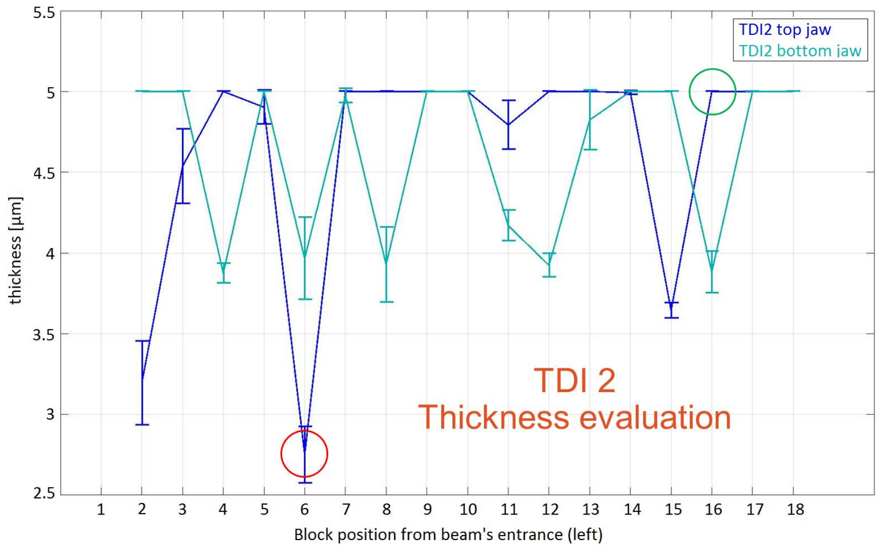

Figure 3.9: Estimation of the titanium layer thickness for TDI2 - hBN, assuming ρ = 2.5 $\mu\Omega$*m (second derivation).

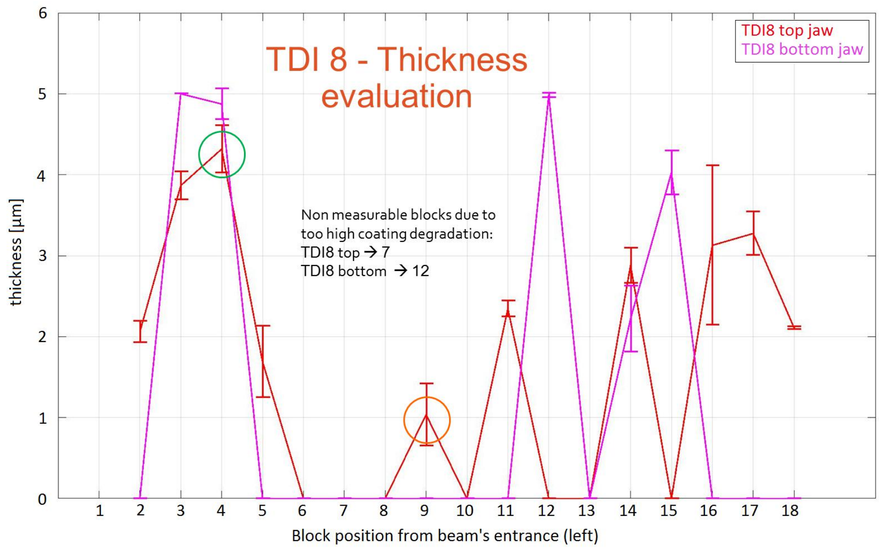

Figure 3.10: Estimation of the titanium layer thickness for TDI8 - hBN, assuming ρ = 2.5 $\mu\Omega$*m (second derivation).

derivations, corresponding also to the low thickness values of the second one, agree with the visibly degraded coating. The same agreement can be found for dual case: not degraded blocks linked with larger thickness and smaller resistivity.

For both the derivations, the first block per jaw met by the beam at the entrance of the TDIs was not measured because its different shape did not suit the designed setup.

The numerical data related to all the measured blocks are reported in Appendix A, together with their positions in the jaws.

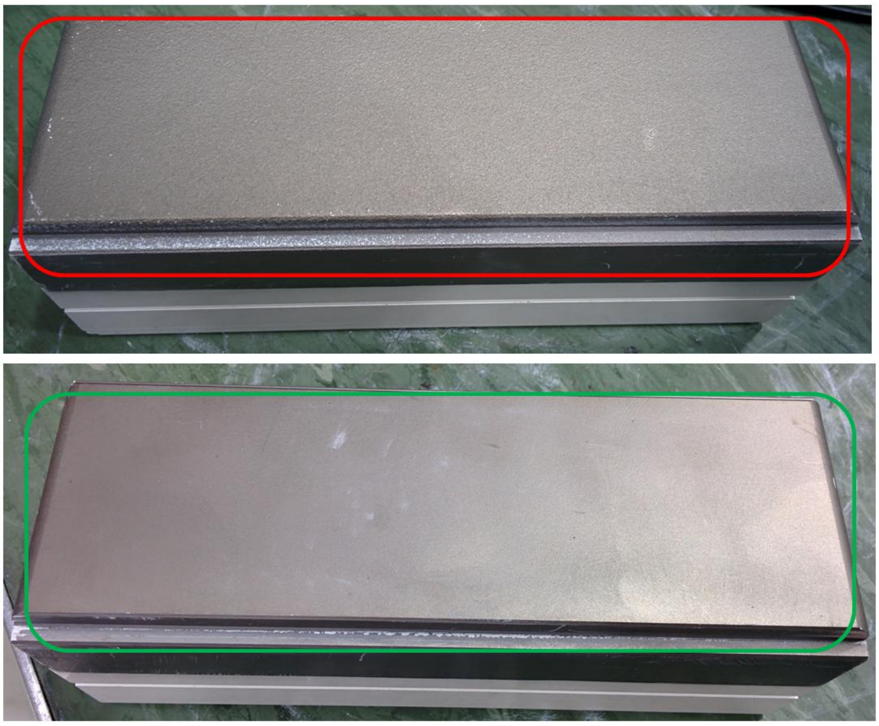

Figure 3.11: Visual inspection of two TDI2 blocks. The coloured circles correspond to the ones in Figure 3.6 and Figure 3.9.

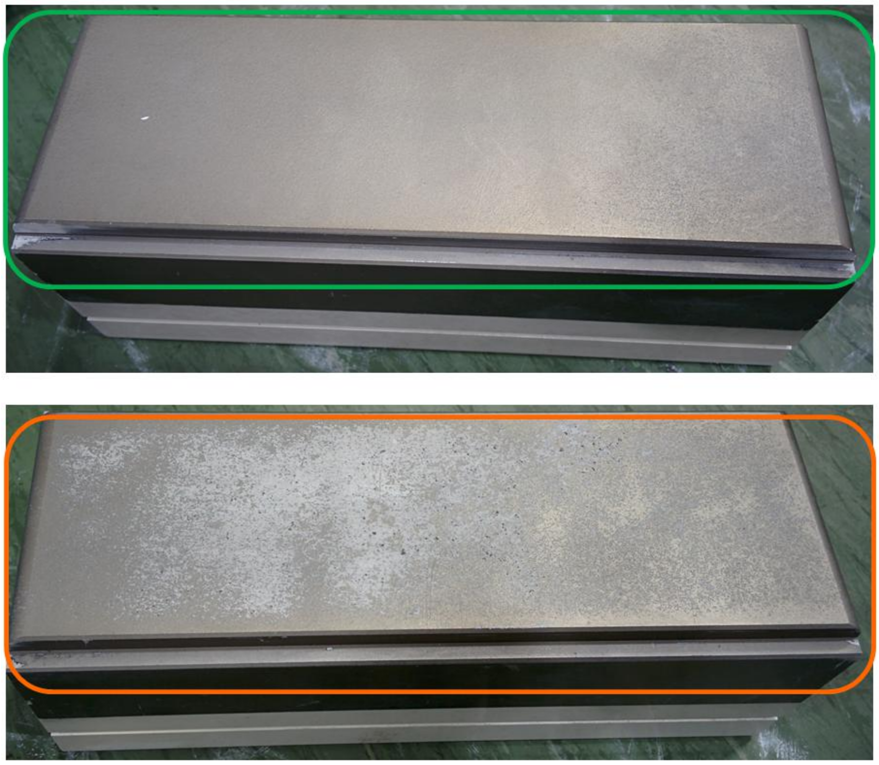

Figure 3.12: Visual inspection of two TDI8 blocks. The coloured circles correspond to the ones in Figure 3.7 and Figure 3.10.

3.3 IW2D numerical simulations

Impedance Wake 2D (IW2D) is a code developed at CERN by N. Mounet to compute longitudinal and transverse beam coupling impedances and wake functions in a multilayer axisymmetric or flat structure that is two dimensional. The number of layers can be in principle anything, and each of them can be made of any linear homogeneous isotropic stationary material. The last layer (which can also be vacuum) should always be modeled with infinite thickness and with low conductivity. The code relies on the analytic computation of the electromagnetic fields created by a point-charge beam travelling at any speed (not necessarily ultrarelativistic) in the whole structure. The formalism for the impedances of a flat structure is developed in Mounet's PhD thesis [6] and is fully described in [19].

The computed impedance with IW2D is the so-called *wall impedance*, which is slightly different from the one called in literature *resistive-wall impedance*: the wall impedance contains the indirect space charge term (perfect conductor impedance) whereas the resistive-wall one does not. This is because the indirect space-charge term is crucial for the low-frequency behaviour (we cannot easily separate its effect from the resistive part). Details on this concept can be found in [20]. The same applies for the wake functions: they also include the indirect space charge.

The data acquired from the resistance measurements on the TDI - hBN blocks were used as input for the IW2D simulations. Each simulation used resistivity and thickness values for a couple of blocks, one belonging to the top jaw and its correspondent of the bottom one. These data were used to model the top and the bottom layers of an IW2D's *Flat Geometry*. The simulation results in terms of impedance, each scaled for one block length, were then summed for each TDI (wall impedance can be summed for structure placed in series, neglecting the interconnection's effect).

For TDI8, a *single-jaw* analysis was also carried out, considering the data for a single jaw per time, and a *Flat Geometry* with a layered structure only on one side of the beam.

3.4 Comparisons between wire measurements and IW2D simulations

The *Wire Method*, initially proposed in [21], allows a good estimation of the energy loss of the bunch in a *Storage Ring* component or in a *Collider* such as the LHC. The basic idea is to replace the beam with a wire where a current pulse is injected, simulating a single bunch. The approximation has some limits: the structure becomes coaxial and allows the TEM mode, which propagates since DC. In these conditions, the energy stored in the wakefields excited in the cavity can propagate towards the extremes of the structure, instead of staying trapped in it. Furthermore, the introduced wire perturbs also the natural modes of the structure. In order to make the wire method more reliable, it can be deduced that the pulse duration must be strictly smaller than the induced fields relaxation time, and the wire must be thin, so that it perturbs the structure as less as possible.

The intuition behind the method lies in the similarity between the field excited by a ultrarealtivistic beam (3.6) and the fundamental one in a coaxial structure (3.7).

$$E_{beam}(r,\omega) = Z_0 H_\phi(r,\omega) = \frac{Z_0 q}{2\pi r} exp\left(-j\frac{\omega}{c}z\right). \tag{3.6}$$

$$E_{coax}(r,\omega) = Z_0 H_\phi(r,\omega) = \frac{const}{r} exp\left(-j\frac{\omega}{c}z\right). \tag{3.7}$$

The *Improved Wire Method* presented in [22] allows to calculate the longitudinal and transverse impedance with the wire method without the need of complex numerical calculations. The improved method allows in fact, with the aid of scattering parameters measurements and the wire method setup, to derive the impedance in the generic case of device not adapted to the adopted instruments (typically VNA at 50 Ω).

The wire method measurements performed during December 2015 *Technical Stop* [23] were compared with the data obtained with IW2D simulations. Concerning the plots reported in this section, it should be kept in mind that the vertical axis is logarithmically scaled and can lead to misinterpretations, considering a factor 2, 3 or 10 discrepancy smaller than it actually is.

As depicted in the three plots for TDI8 (Figure 3.13, Figure 3.14, Figure 3.15), the two derivations (green and blue lines) are practically coincident. This is easily justifiable, considering that a large part of TDI8 blocks was not measurable for the lack of residual coating. Those blocks, because of the derivations boundary conditions, have been modeled in the same way for both the derivations: without the titanium layer and with the hBN bulk directly exposed to the beam. Because of this, they gave the largest contribution to both the curves.

As for the TDI2 plot (Figure 3.16) we can observe that the second derivation's curve (blue dashed line) is shifted from the first derivation's one (green solid line), being closer to the

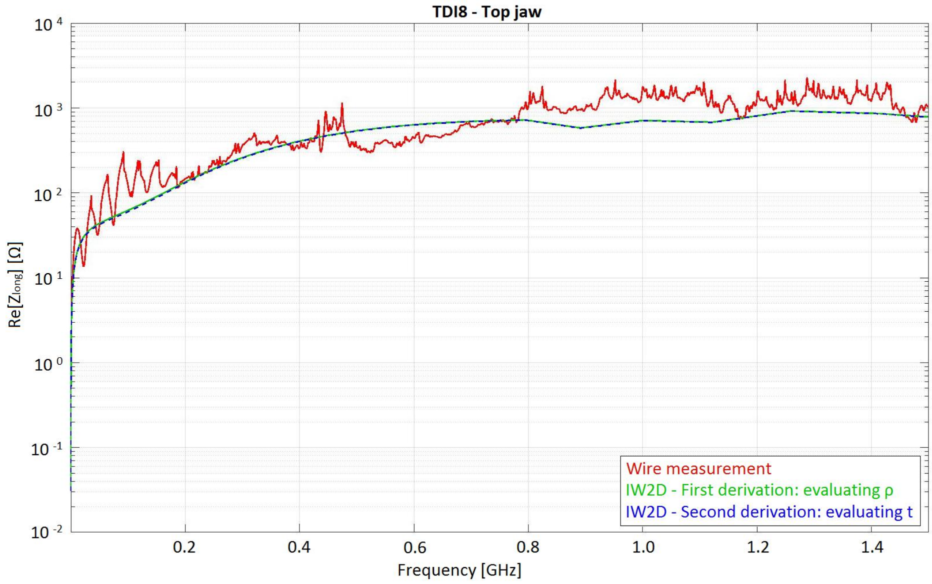

Figure 3.13: TDI8 top jaw. Comparison between IW2D simulations (first derivation in green, second derivation in blue) and wire method measurements (red). On the vertical axis the real part of the longitudinal impedance is logarithmically scaled.

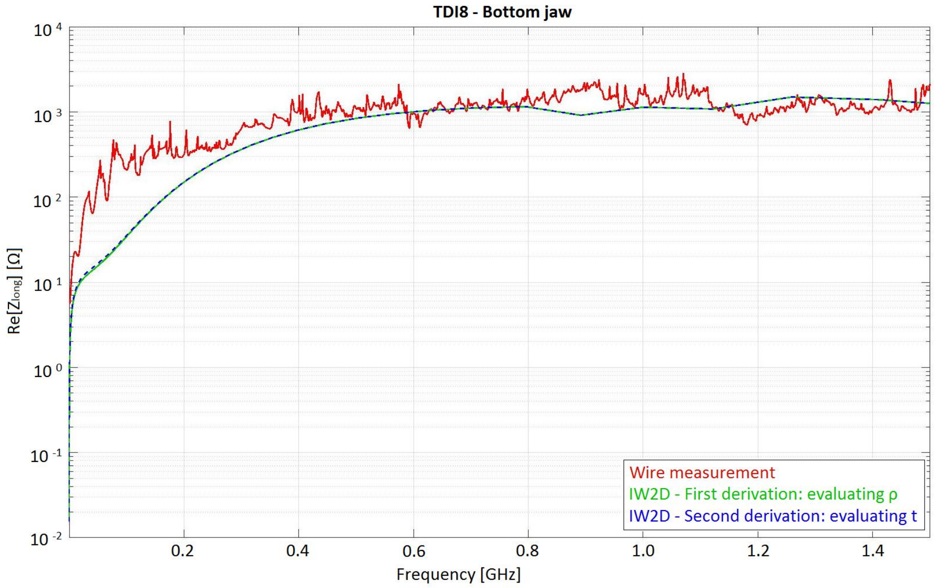

Figure 3.14: TDI8 bottom jaw. Comparison between IW2D simulations (first derivation in green, second derivation in blue) and wire method measurements (red). On the vertical axis the real part of the longitudinal impedance is logarithmically scaled.

measurement one (red solid line). Differently from TDI8, almost all the TDI2 blocks were measurable and the effect given by the beam exposed hBN is not as influential as it was for TDI8, letting other factors play also an important role. This distance between the two derivations for TDI2 let us suppose that in this frequency range a variation of the Titanium

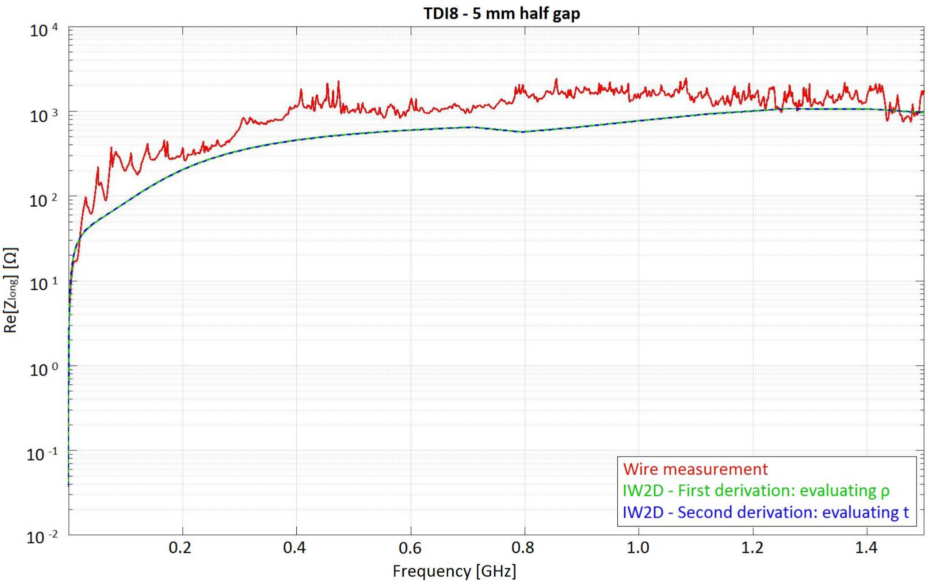

Figure 3.15: Comparison between IW2D simulations (first derivation in green, second derivation in blue) and wire method measurements (red) for TDI8 at hgap = 5 mm. On the vertical axis the real part of the longitudinal impedance is logarithmically scaled.

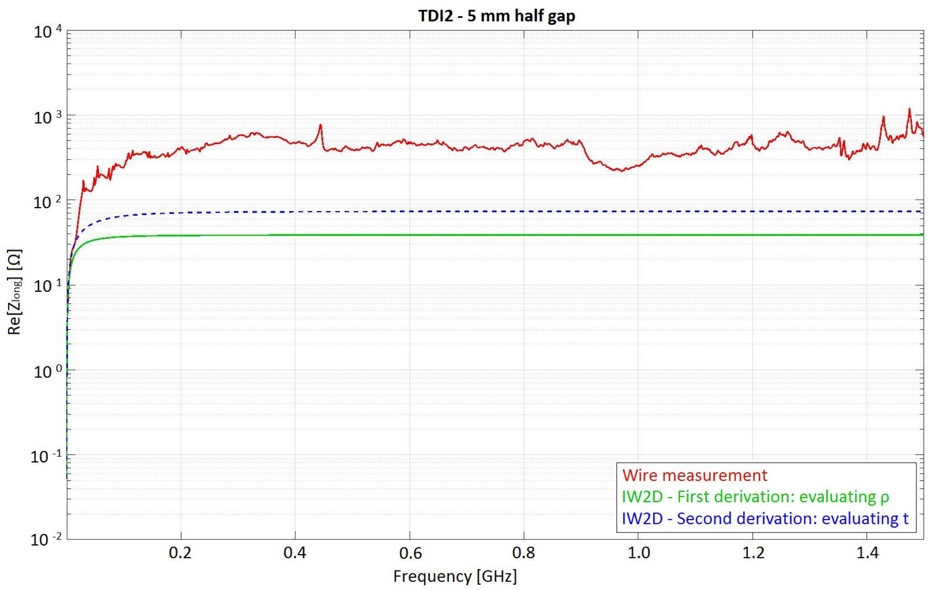

Figure 3.16: Comparison between IW2D simulations (first derivation in green, second derivation in blue) and wire method measurements (red) for TDI2 at hgap = 5 mm. On the vertical axis the real part of the longitudinal impedance is logarithmically scaled.

layer thickness has more influence than a variation of its resistivity: a small thinning exposes a larger amount of non conductive hBN to the beam, degrading the performance more than a small deterioration of the average layer quality. hBN effects in terms of longitudinal impedance are already visible in the TDI8 plots, especially when compared to the TDI2 ones.

The observable discrepancies between simulations and measurements can be justified considering that in IW2D the jaws are approximated with infinitely extended planar structures and with no discontinuities in the beam propagation direction. These discontinuities were located between each block and mostly between the blocks supports (each support holds three absorbing blocks). They are probably also the cause for the low frequency oscillations, that are especially visible in TDI8 plots.

The reported plots are all derived from studies and measurements at hgap = 5 mm. Their repetition at hgap = 10 mm led to analogous considerations.

Summarizing the results of the chapter, we could impute the coating degradation and the following hBN exposure to the beams to be the main responsible of the lack of the TDI performances, in terms of impedance. The next two chapters will deal with the TDI currently installed in the LHC, with copper coated graphite blocks. A large improvement of performance was achieved compared to the TDI - hBN, but it did not completely satisfy the expectations we initially had.

Chapter 4

TDI - Graphite

In this chapter we will firstly introduce the new blocks that replaced the hBN based ones and that are currently installed in the LHC.

Afterwards, we will present the *Machine Developement* (MD) carried out in May 2016 to acquire data on the TDI - Graphite. The data, gap and tune values, were later processed with MatLab to cross out the noise and evaluate the tune shifts corresponding to the main jaws positions.

Using new IW2D computations, tune shift contour plots were later drawn as a function of the coating's resistivity and thickness, for different half gaps. These plots were used to visually estimate the discrepancy between the expected shift and the one we had in the machine. However, as we will mention in the following and investigate in chapter 5, the geometry of the TDI was also another important source of mismatch, since IW2D does not consider it in its numerical computations.

4.1 TDI - Graphite's blocks

During 2015/16 winter shutdown, the TDIs blocks were uninstalled and substituted with others, which had different characteristics. Since they were three times longer (Figure 4.1), 6 blocks per jaw were used instead of 18, as it was for run 2015 with hBN blocks.

In spite of the number and the dimension changes, the biggest impact of this substitution is given by the different materials and layer structures, compared in Table 4.1 and Table 4.2.

The top layers' materials resistivity is the one that was used for our numerical computations but it does not correspond to the textbook bulk material resistivity: the values reported and adopted consider in fact the imperfect coating depositions and the stress experienced during

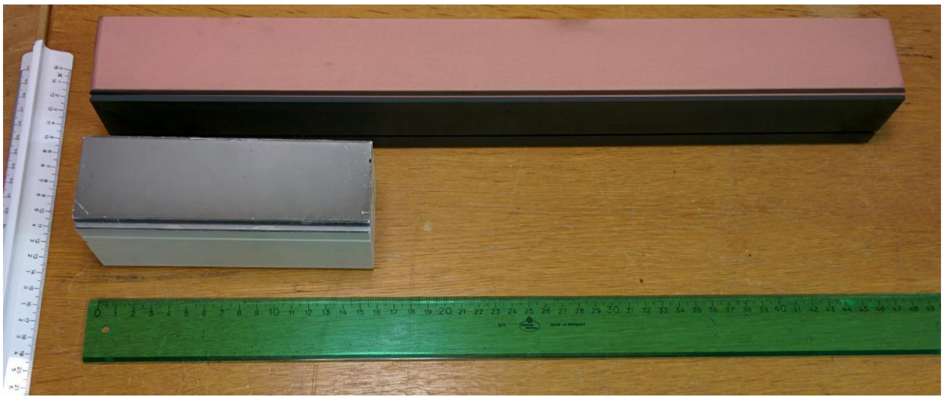

Figure 4.1: Visual comparison between an hBN bulk block and a graphite bulk block.

	Material	Thickness	Resistivity
Layer 1	Titanium	$5\mu m$	$2.5\ \mu\Omega\ m$
Layer 2	hBN	$54\ mm$	dielectric ($\varepsilon_r = 4.5$)

Table 4.1: Layer structure of the TDIs' blocks used during LHC run 2015. The layers are numerated starting from the one closest to the beam.

	Material	Thickness	Resistivity
Layer 1	Copper	$2\mu m$	$26\ n\Omega\ m$
Layer 2	Titanium	$0.5\mu m$	$2.5\ \mu\Omega\ m$
Layer 3	Graphite	$54mm$	$15\ \mu\Omega\ m$

Table 4.2: Layer structure of the TDIs' blocks in use nowadays. The layers are numerated starting from the one closest to the beam.

the machine operations, which could lead to degradations as impurities and inhomogeneities in the coating.

Since the graphite is a better conductor than hBN, it was expected a smaller field penetration in it, with a consequent lower warming. This would bring other advantages: lower beam energy losses, lower blocks degrading, lower effects on machine parameters, such as tune shift and phase shift.

The bulk was not made with very highly conductive materials on the first place because there are strict requirements on the material's thermal and chemical stability in case of beam impact. Materials such as copper would simply not be suited to absorb mis-injected beams, and may also outgas, compromising the vacuum.

4.2 MDs data acquisition and processing

During the previous LHC run, the TDI had a strong influence on both tune and phase. The Impedance Team was therefore on charge of performing some experiments on the operative LHC during the first weeks of run 2016, to check the performances of the upgraded TDIs. In other words, the team was allowed to move the collimators directly from the CCC (*CERN CONTROL CENTER*), in order to gather important data for further analysis.

The CCC (Figure 4.2) combines control rooms for the laboratory's accelerators, the cryogenic distribution system and the technical infrastructure. It holds 39 operation stations for four different areas: the LHC, the SPS, the PS complex and the technical infrastructure.

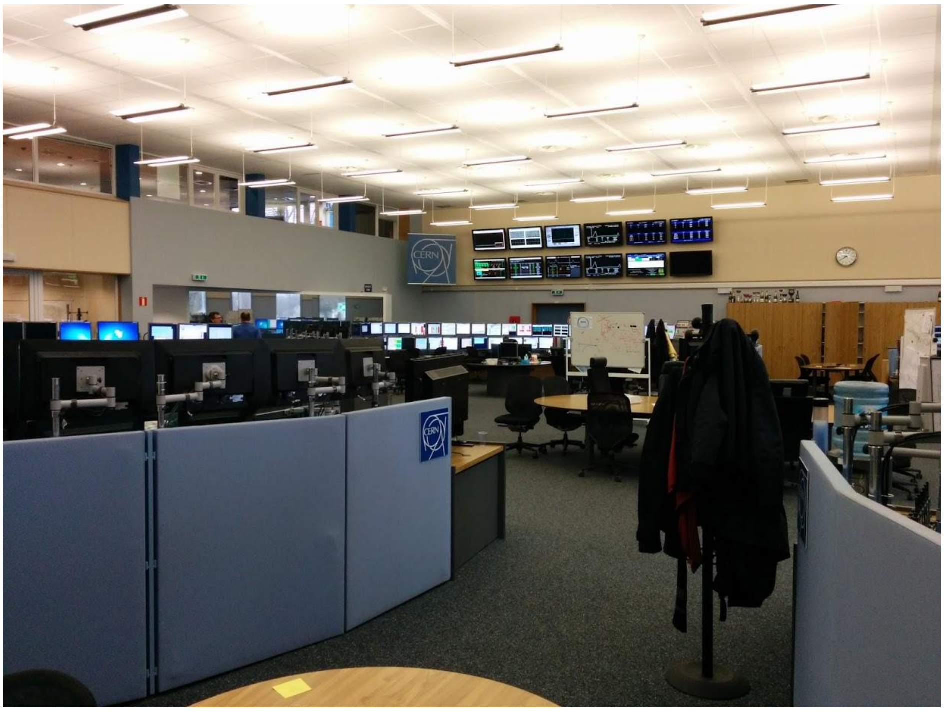

Figure 4.2: *CERN CONTROL CENTER*.

To verify the TDIs impact on the machine parameters, they have been observed with all the other collimators opened, and varying the apertures of TDIs' jaws. The most interesting positions were the working position (hgap = 3.8 mm), the maximum closure position (hgap $\approx$ 2.2 mm) and the parking position (hgap $\geq$ 50 mm). The maximum jaws closure was established looking at the beam's intensity: a smaller aperture immediately provoked a dump. The collimators were moved by the CCC operators, while the variables were observed from any CCC terminal with the tool called *Timber*.

In order to do some performance comparison between TDI - hBN and TDI - Graphite, in the present section we will also provide some examples of the former one, such as the one in

Figure 4.3, reporting TDI8 gap and Beam 2 Vertical tune during run 2015.

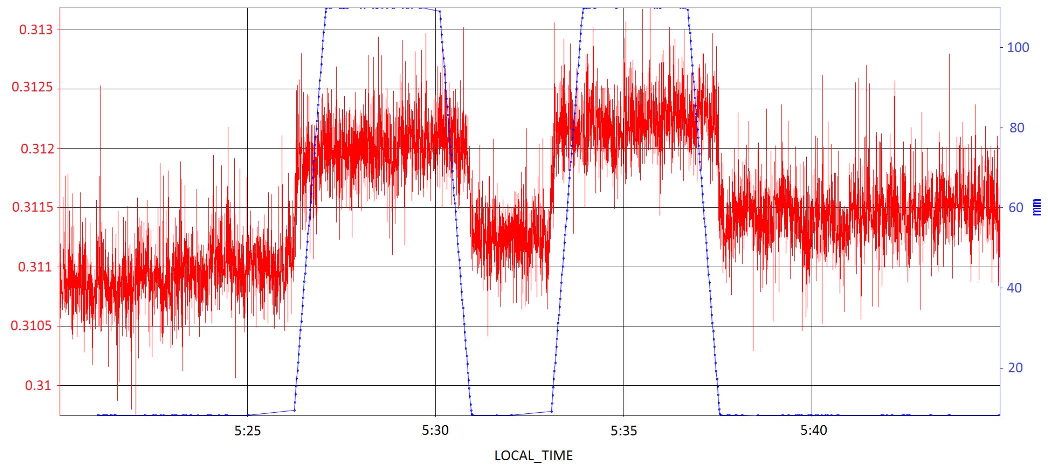

Figure 4.3: Beam 2 Vertical tune (red line) and TDI8 gap (blue line) on 9 August 2015, between 05:20:00 and 05:45:00.

The LHC tune measurement is performed with the so called BBQ (*Base Band tune*). This system is basically composed by the *Pick-Up* and a diode-based circuit. The former is a beam position monitor composed by two electrodes. The latter takes advantage of the differential signal obtained from the Pick-Up's electrode to evaluate the beam transverse position (further details can be found in [24]). Observing the beam's displacement at the same machine position for several turns is then possible to derive the transverse motion's spectrum, whose main component corresponds to the machine's tune.

Timber offers also the chance to post-process the data: in our case the averaging on a given time interval was used because it helped to cross out a large part of the high frequency noise (Figure 4.4 shows the same data of Figure 4.3, after the averaging).

Before adding the time averaging, a strong tune shift was already clearly visible, in correspondence of the jaws' movements, for run 2015. On the other hand, looking at Figure 4.5 (run 2016), the tune shift (blue) related to the gap movement (green) is not clearly visible, even after a time averaging. Therefore, it was decided to export the data and post process them in a more controlled way with MatLab. The steps of the post processing algorithm are given in the following.

1. Since tune and gap had different sampling times and these were often not perfectly constant, as a first step, the points of both the functions were interpolated, letting both their time vectors be equally-spaced.

2. The second step was to exclude the tune's linear drift with time. In order to do so, the

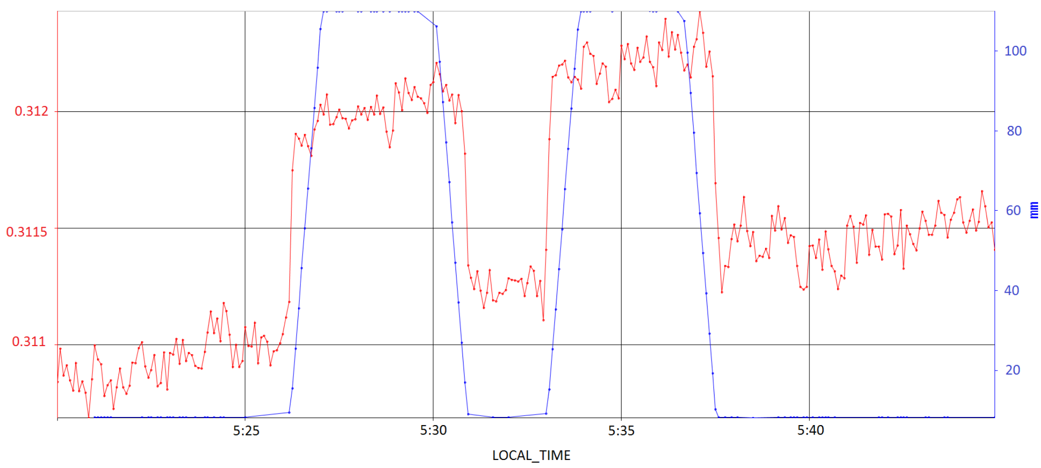

Figure 4.4: Beam 2 Vertical tune (red line) and TDI8 gap (blue line) on 9 August 2015, between 05:20:00 and 05:45:00, with 5 seconds time averaging post processing.

tune first order polynomial interpolation was subtracted from the tune itself. The result was then shifted to the original tune mean value, summing it as a constant to all the vector's elements.

3. The time averaging on Timber gave as a result a number of points that was a fraction of the original amount. This happened because with Timber N points were simply substituted with one, correspondent to their mean value. In the designed algorithm it was chosen to adopt a *Moving Average* filter, thus excluding only some initial and ending points and obtaining more resolution in the center interval.

4. The last step consisted in averaging the tune separately when the gap was open and when the gap was closed. Since the gap does not change instantaneously and not always between the same values, to cross out the transition parts some thresholds were established. The thresholds were automatically set where the gap became larger than a certain percentage of its minimum values (while it was closing) and where it became smaller than a certain percentage of its maximum values (while it was opening). The percentage was gradually increased and the procedure repeated until the expected number of open-close steps (set as a parameter by the algorithm user) was detected. The tune values between the thresholds were then excluded, since they represented transitions between the open positions and the closed ones, while the others were separately averaged in each remaining interval. The differences between these mean values were the tune shifts caused by the considered TDI at closed gap, assuming the open gap as a reference. The mentioned percentages were increased starting from 1%

since lower percentages allowed to exclude as many tune transitions values as possible, obtaining a more realistic estimation.

Ideally, in order to compare the results with the ones of other time intervals, the closed gap values should be as similar as possible for each open-close cycle (the open gap values are less important since after a few millimeters the jaws are basically invisible for the beam, in terms of tune).

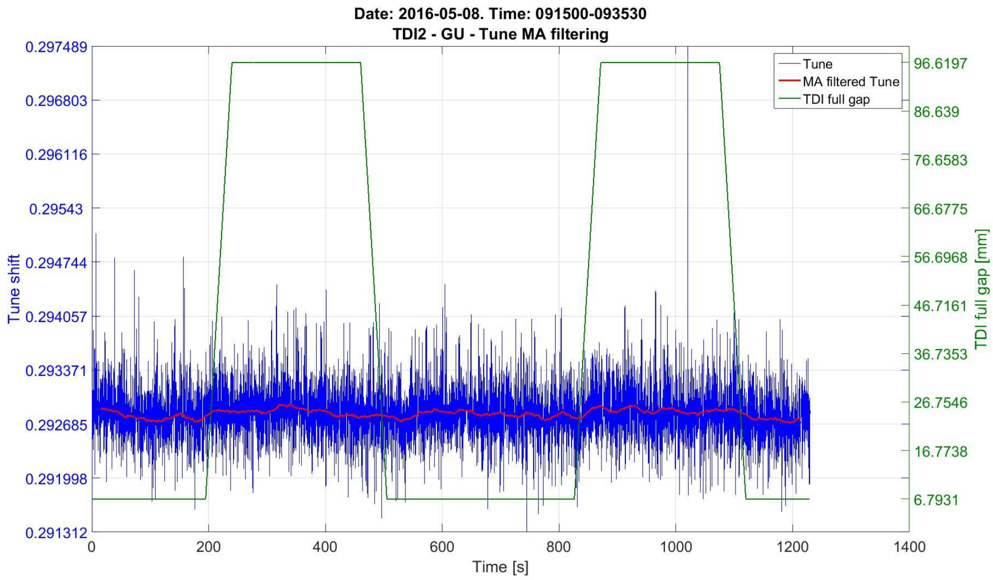

Figure 4.5: TDI2 full gap upstream (green), Vertical tune shift (blue), MatLab filtered Vertical tune shift (red). Tun and gap were collected with Timber, and they refer to 9:15:00 - 9:35:30 on 8 May 2016.

As an example, some MatLab plots comparing the tune data before and after the post processing are reported in Figure 4.5 and Figure 4.6. Both of them refer to the same time interval of run 2016. Some derived tune shift values are reported in Table 4.3, together with LHC data acquisition date and time.

From the comparison between Figure 4.5 and Figure 4.4 we notice that in run 2015, that is when hBN blocks were installed, the shifts were large enough to be easily spotted without any kind of post processing. On the other hand, in run 2016 the tune shifts (blue) corresponding to the gap movements (green) were impossible to be detected without the aid of a post processing like the one we implemented and described above.

Large part of this section's pictures and data were collected and used for one of the *TDIS Meeting* [25].

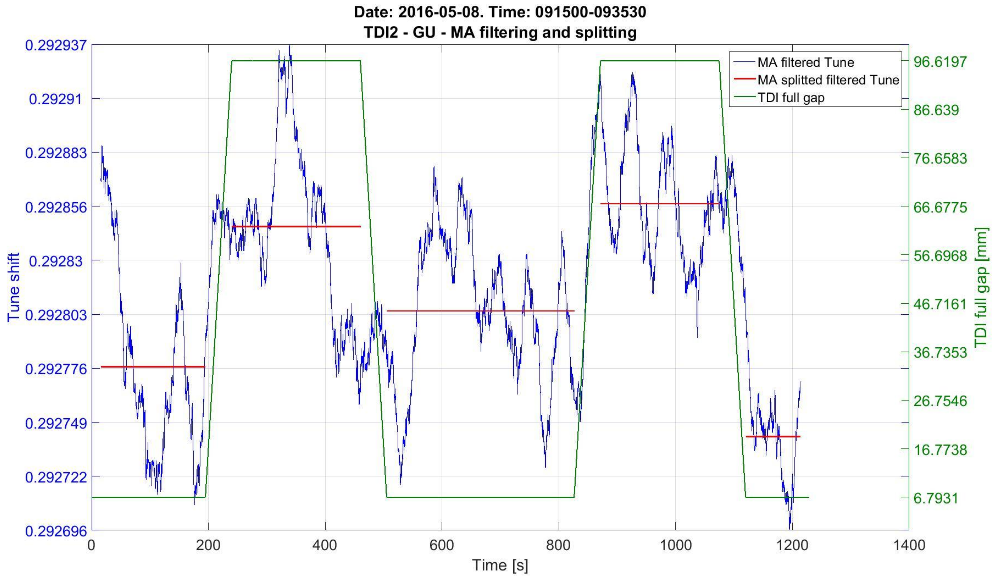

Figure 4.6: TDI2 full gap upstream (green), filtered Vertical tune shift (blue), filtered Vertical tune shift mean levels at open and closed gap (red). tune and gap were collected with Timber, and they refer to 9:15:00 - 9:35:30 on 8 May 2016.

Date and time	TDI	Vertical ΔQ	Open-Close cycles	Closed jaw mean hgap
8 May 2016 8:11:30 - 8:30:00	TDI2	$(7.5 \pm 1.8)10^{-5}$	2	3.8 mm
	TDI8	$(11 \pm 0.4)10^{-5}$	2	4.1 mm
8 May 2016 8:33:30 - 8:45:00	TDI2	$(3.5 \pm 0.6)10^{-5}$	1	3.8 mm
	TDI8	$(6.7 \pm 1.4)10^{-5}$	1	4.1 mm
8 May 2016 9:15:00 - 9:35:30	TDI2	$(7.0 \pm 1.6)10^{-5}$	2	3.1 mm
8 May 2016 9:35:00 - 9:51:00	TDI2	$(4.9 \pm 0.7)10^{-5}$	2	3.1 mm
9 April 2016 10:27:00 - 10:52:00	TDI2	$(1.3 \pm 0.1)10^{-4}$	3	2.2 mm
	TDI8	$(1.2 \pm 0.2)10^{-4}$	3	2.5 mm
9 August 2015 5:20:00 - 5:45:00	TDI2	$(1.6 \pm 0.2)10^{-4}$	2	5.2 mm
	TDI8	$(8.7 \pm 0.3)10^{-4}$	2	4.1 mm

Table 4.3: TDIs tune shift values derived with the described MatLab post processing.

4.3 Tune shift analysis as a function of the coating's resistivity and thickness

The study presented in this section was carried out with other IW2D simulations and MatLab post processing using the layer structure of the TDI - Graphite (Table 4.2).

The aim was to understand to what extent the tune values obtained in the previous section agreed with the expected ones and, in case they did not, consider the possible sources of mismatch, first of all the coating degradation.

The new IW2D simulations were parametrized changing hgap, resistivity and thickness of the copper layer, that is the beam closest one. Resistivity is an intrinsic material parameter: we used it as a variable because the coating deposition was not necessarily perfect and the stress which it underwent during the machine operations affected its purity and uniformity. A resistivity higher then the nominal one for a pure copper bulk was then adopted as a reference for the top layer. The stress induced by the LHC operations was also the justification to assume the layer thickness as the other variable.

The IW2D parametrized simulations results in terms of impedance were processed with MatLab to evaluate the TDI tune shift and to graphically present the results.

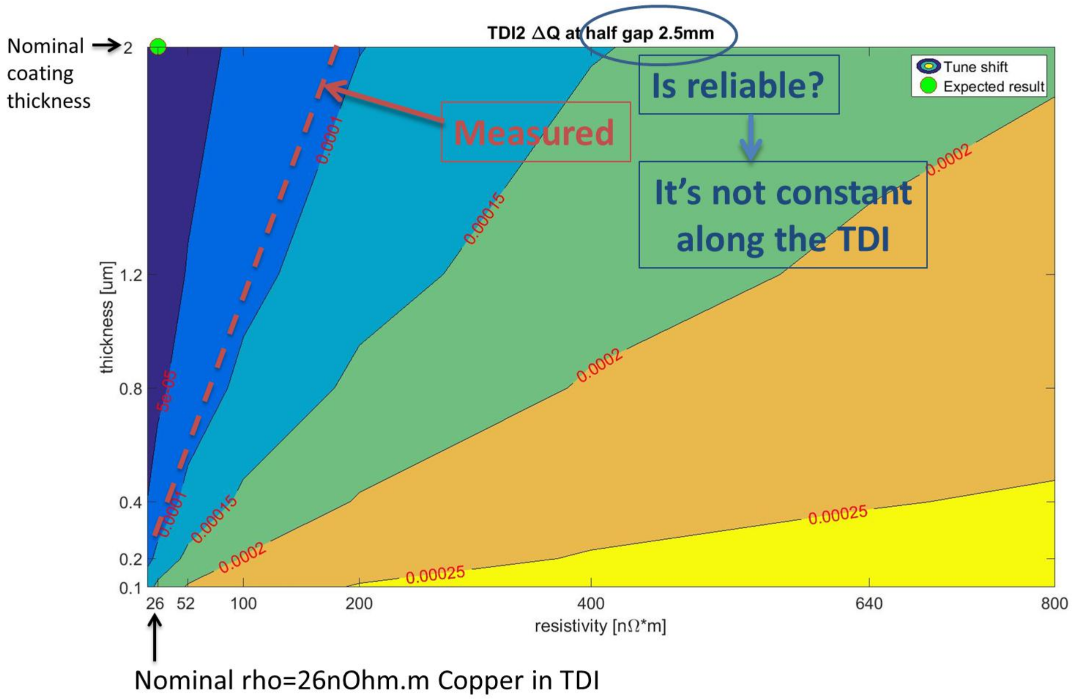

Figure 4.7: TDI2 tune shift contour plot as a function of copper layer's resistivity and thickness at hgap = 2.5 mm.

Expected resistivity and nominal design thickness were adopted as a reference for the analysis: a displacement from this reference might imply an unforeseen high coating degradation which could justify displacement from the expected tune values.

The first picture (Figure 4.7) shows a fan of curves with constant tune shift lines, as a function of the layer resistivity and thickness, for TDI2, with hgap = 2.5 mm. Nominally, we should have 2 μm thickness and 26 nΩ*m resistivity. A green dot was placed at these coordinates, and it corresponds to $\Delta Q \approx 2.5 \times 10^{-5}$. Nevertheless, most of the values obtained from the MD (section 4.2) and represented with the red dashed line were quite far from the green dot. On the other hand, this results did not take into account that the Timber gap values could refer to the gap aperture either at the beam entrance or at the beam exit, called *Gap Upstream* and *Gap Downstream*, respectively. The difference between these values could also be half millimeter, and it is not too surprising since the jaws were almost 3 meters long.

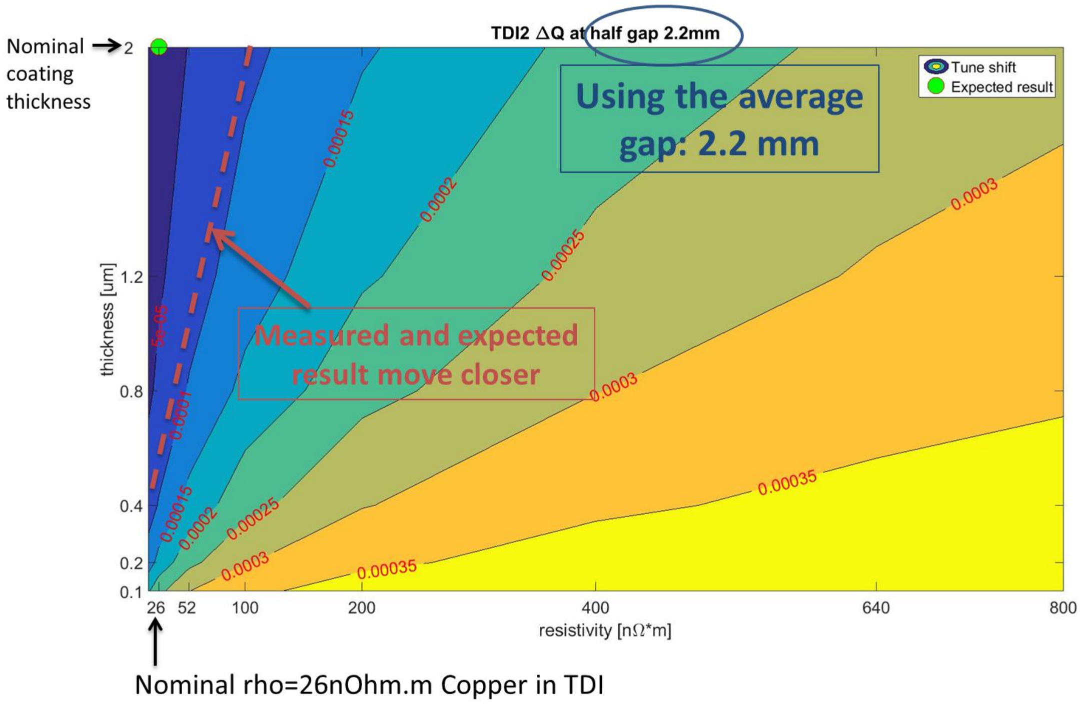

Figure 4.8: TDI2 tune shift contour plot as a function of copper layer's resistivity and thickness at hgap = 2.2 mm (i.e. the upstream and downstream mean value).

Drawing again the same contour plots using as gap the average between upstream and downstream, the dashed line (the measurements) and the green dot (the expected result) approached considerably (Figure 4.8). The difference between the tune shift values is about the same. However, this time the measurement corresponds to $(\rho;\, t)$ coordinates closer to the nominal ones. In other words, assuming that measurement and simulations are reliable, the layer appeared less degraded than in the previous plot (Figure 4.7), where we were not considering that upstream and downstream gaps were different.

The tilting given by the difference between upstream and downstream was considered using their mean value. We can see this approach as a first order approximation, and we moved to a second order one with a tilting quantization, as represented in Figure 4.9.

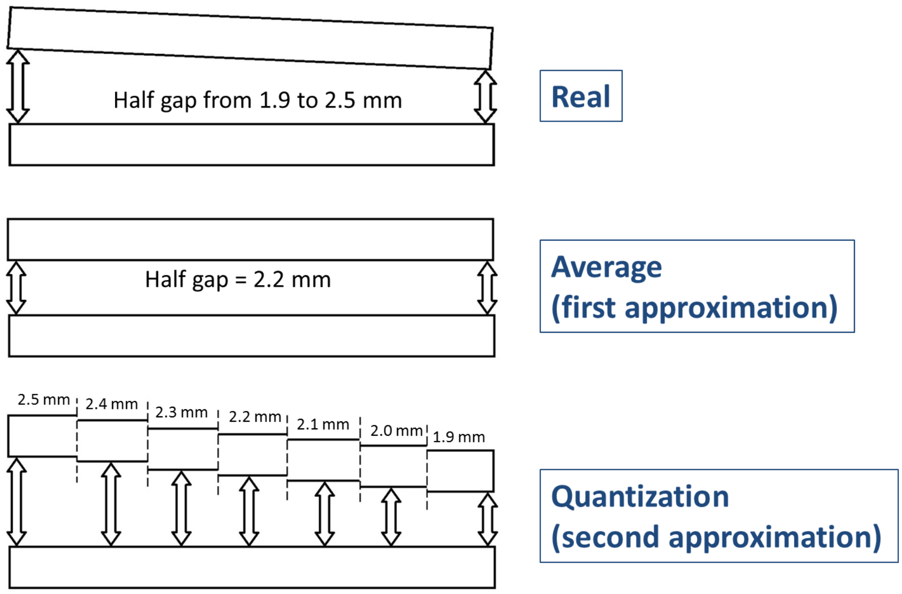

Figure 4.9: From the top: top jaw tilting, its first order approximation, its second order approximation.

The sharp gap variations are not considered in IW2D, since it does not take into account the full geometry of the structure. The result in term of impedance, and afterwords of tune shift, was obtained scaling the impedances for the length of the respective piece instead of the full TDI's one (in Figure 4.9 the piece length is 1/7 of the total length), and summing the contributions.

The result is shown in Figure 4.10. Again here, comparing with the previous case, we observed that measurement and expected result approached. We could then deduce that the segments with smaller gap have more influence than the ones with larger gap, otherwise we would have obtained the same results of the first order approximation.

One last consideration that decreased the distance between green dot and dashed line was the chance of an error in the gap measurement. In Figure 4.11 half millimeter error on the half gap was supposed. However, it should be stressed that, as it was later confirmed, 1 mm gap error was an overestimation of the instrumentation maximum error, that should be around one or two hundreds of micron.

Most of this section's plots were produced and presented at one of the *Hadron Synchrotron Coherent effects* (HSC) Section Meetings [26] and one of the TDIS Meeting [25].

In spite of the residual displacement between measurements and simulations, the conclusions

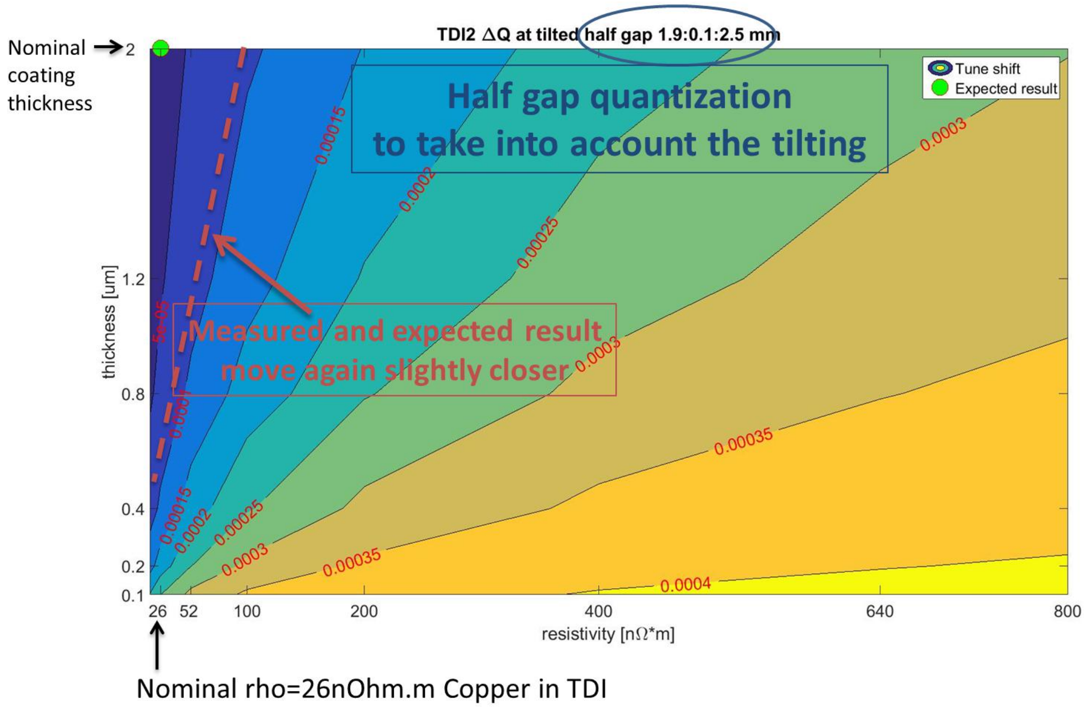

Figure 4.10: TDI2 tune shift contour plot as a function of copper layer's resistivity and thickness, with half gap quantization in seven segment: 0.1 mm step between 1.9 mm and 2.5 mm (the second order approximation).

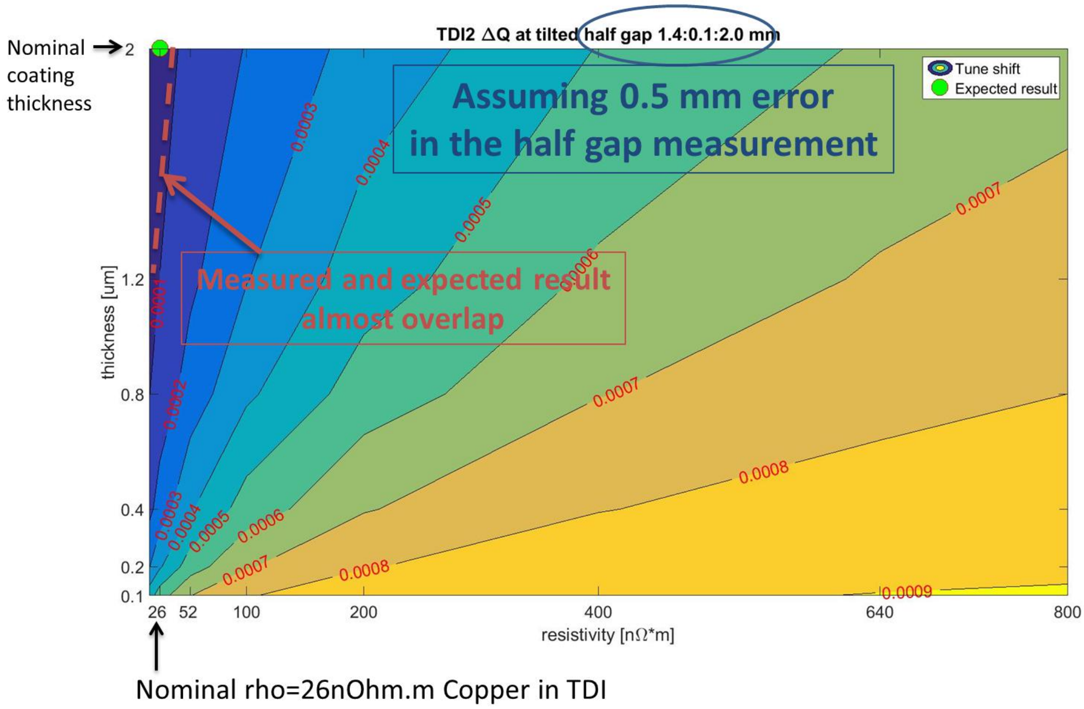

Figure 4.11: TDI2 tune shift contour plot as a function of copper layer's resistivity and thickness, with half gap quantization in seven segment: 0.1 mm step between 1.4 mm and 2.0 mm (the second order approximation with 1 mm gap error).

we drew were that the coating was probably in good conditions: the hypothesis we made was that the source of the residual mismatch was that IW2D computes only the wall impedance, not taking into account the real TDI geometry and its discontinuities. The electromagnetic time-domain simulation with a 3D model of the TDI are reported in the next chapter, and were run in order to confirm the key role of the TDI geometry to estimate impedance and tune.

Chapter 5

CST simulations of the TDI - Graphite

At the beginning of this chapter *CST Studio Suite* (CST in the following) [27] will be briefly presented, together with some theoretical connection with what we defined back in section 2.2. Following that, the procedure to implement asymmetrical displacement from *Mirrored* structures of a CST 3D model is described. This procedure was used to upgrade the TDI 3D model, allowing asymmetrical jaws positioning with respect to the beam.
The other sections of the present chapter contain comparisons of CST simulations results in terms of impedance and, if followed by MatLab post-processing, of tune shifts as well.
The chance to move only one jaw close to the beam was required to complement the investigation we carried out in the previous chapter, concerning the behaviour of the TDI - Graphite. According to our supposition, the remaining mismatch between measurements and simulations was given by the geometry of the TDI, not taken into account by IW2D. Letting one jaw far from the beam, and the other one close, the wall impedance should be half compared to the case where both the jaws are close to the beam. The impedance computed with CST did not show this behaviour for the TDI model, and we could conclude that the geometrical factor played a key role.
Jaws segmentation was another major upgrade, recently added by B. Salvant (CERN - BE department, who also provided the original model we started to work with). These segmentations were added because it was expected that they could contribute to the geometrical factor, and it was verified in section 5.3, with the asymmetrical displacement tests.
Finally, in section 5.4 we investigated a recent phenomenon observed in the LHC: some degradations in the vacuum were detected when retracting the jaws to the parking position. The possibility of a TDI sub-component outgassing was therefore considered.

5.1 CST - Wakefield Solver

CST is a commercial software for 3D electromagnetic simulations. In our studies, *Particle Studio* environment's *Wakefield Solver* was widely used. The Wakefield Solver employs a time domain excitation of the structure in order to derive the wakefields and, consequently, the beam coupling impedance, with the aid of a Discrete Fourier Transformation (DFT).

CST adopts a single-bunch approach. Therefore, the consideration we made in section 2.2 for test charge and source charge should be adapted to a bunch. Indeed, the CST time domain analysis results will not be the wakefields as we defined them: CST results are called *wake potentials*, which are defined as the wakefields convolution with the bunch profile $\lambda(z)$:

$$\begin{aligned} W_{pot}(x_S,\, y_S,\, x_T,\, y_T,\, z_T) &= (W * \lambda)(z_T) = \\ &= \int_{-\infty}^{+\infty} \lambda(z_T - z')\, W(x_S,\, y_S,\, z_S = z',\, x_T,\, y_T,\, z_T)\, dz'. \end{aligned} \tag{5.1}$$

In CST, we adopted a gaussian distribution $\lambda(z)$:

$$\lambda(z) = \frac{1}{\sqrt{2\pi}\sigma_b} e^{-z^2/(2\sigma_b^2)}. \tag{5.2}$$

Integrating in dz' we cross out the dependency on z_S, leaving only 2 coordinates for the source. According to this, in CST the beam is directed on a straight path identified by two coordinates lying on the plane perpendicular to its direction. These coordinates correspond to our x_S and y_S, assuming the beam moving along a direction perpendicular to the z axis. Furthermore, the wake potential is evaluated on an axis that can be placed parallel to the beam's one: its xy coordinates match to our x_T and y_T. (5.1) is then evaluated for z_T that moves from the bunch until a certain distance, defined as *Wakelength*, that is one of the parameters that can be set before the simulation starts.

Since the Wakelength affects the observed time window, it will also be responsible of the maximum frequency resolution that we can attain. The larger the Wakelength, the better the frequency resolution but also the longer the simulation. Approximately, the simulation time grows linearly with the Wakelength. The maximum DFT points used by CST can be set in the section *Specials*, of the Wakefield Solver setup. Differently from the Wakelength, the maximum number of DFT points has a small impact on the total simulation time. As a rule of thumb the adopted Wakelength should be chosen much larger than the *bunchlength* σ_b, and it should also allow the wake potentials to decay approximately to zero. If oscillations are still dominant in them (as it can be in the case of a strongly resonant structure) either a convergence test should be performed or the simulation should be repeated with a larger Wakelength.

Because of the difference between wake potentials and wakefields, the impedance is derived starting from the wake potentials taking into account the bunch spectrum $\Lambda(\omega) = \mathscr{F}[\lambda(z)] = e^{-\sigma_t^2\omega^2/2}$, where $\sigma_t = \sigma_b/v$, $\mathscr{F}$ is the Fourier transformation operator and $*$ the convolution symbol:

$$\begin{aligned} Z(x_S, y_S, x_T, y_T, \omega) &= \mathscr{F}[W] = \\ &= (\mathscr{F}[W]\, \mathscr{F}[\lambda])\, \frac{1}{\mathscr{F}[\lambda]} = \\ &= (\mathscr{F}[W * \lambda])\, \frac{1}{\mathscr{F}[\lambda]} = \\ &= \frac{\mathscr{F}[W_{pot}]}{\Lambda}. \end{aligned} \tag{5.3}$$

Wake potentials are computed and plotted as a function of s, that is the longitudinal distance from the bunch. In order to attain the frequency dependency after the transformation, we should also involve the bunch speed. In our simulations, the relativistic velocity factor β was approximated to unity, thus v = c. Hence, in CST impedance is computed as far as the bunch spectrum (which is also gaussian) allows it. More in details, the maximum frequency is set where the bunch spectrum decays to -20 dB of its maximum values:

$$\begin{aligned} f_{max} &= c\frac{\sqrt{ln 100}}{2\pi\sigma_t}. \\ f_{max}\,[GHz] &\approx \frac{100}{\sigma_b[mm]}. \end{aligned} \tag{5.4}$$

Instead of using the actual bunchlength, sometimes we set a shorter σ_b to observe also the impedance at higher frequencies. Our interest in the higher part of the spectrum is related to intrabunch modes (given by the perturbations of the longitudinal distribution of the bunch) which can have frequencies higher than the f_{max} we would obtain with the actual σ_b.

What described above corresponds to the integration method that CST calls *Direct*, that is the one we mainly adopted in our simulations. One of the other methods available in CST and that we also used is the *Indirect interfaces*. It can be adopted when dealing with ultrarelativistic beams and concave structures (more details on the method can be found in [28]).

If the electric field tangential components cancel at the integration boundaries, CST can also employs the Panovsky-Wenzel theorem [29] to derive the transverse wake directly from the longitudinal one [30], as in (5.5). This theorem is also used for the wire method measurement we briefly presented in section 3.4 to calculate the transverse impedance from the measured longitudinal one.

$$W_{pot_t}(z_T) = -\bigtriangledown_t \int_{-\infty}^{z_T} W_{pot_l}(z')\, dz'. \tag{5.5}$$

5.2 3D model updating from asymmetrical translations

Since the complete 3D TDI model was too complex to be directly simulated, many simplifications were made when the first simulations were performed. During the following years the model underwent several modifications in order to gain accuracy, reliability when simulations were compared to measurements, and also to meet the real TDI upgrades. As already mentioned, the model we started to work at the beginning of this chapter's upgrades and analysis was provided by B. Salvant (CERN - BE department).

The present section describes how we upgraded the TDI model to allow asymmetrical jaws displacements. We will discuss some CST features, some of their advantages but also one disadvantage that prevented a simple way to achieve the desired upgrade. Beside rebuilding the model from the beginning, an alternative way to upgrade the model was found and used for most of the TDI moving parts (jaws sub-components or jaws related components). The limitation of this alternative method is that it only allows translation on a single axis. The TDI components that modified their shapes or inclinations depending on the displacement of their associated jaw were therefore deleted and modeled again from the beginning.

A widely used CST feature is the chance to create parameters, which can be used while modeling the physical structure of a device. The user can create elements whose positions and shapes are directly parametrized or dependent on functions of those parameters. Updating one of the parameters from the *Parameter List* processes the whole *History List* since the beginning with the updated parameter's value. The fact that the entire History List (menu *Edit*, section *Modeling*) is processed again has a fundamental importance. If it was not so, when a user creates an object and after he/she performs actions relatively to it (such as a complementary filling for instance), the parameter update would only lead to the object modification and not affect the relative actions that followed its creation (the filling would not change accordingly, with undesired overlapping or empty sectors as a consequence). In the TDI model the parametrization was widely used: the jaws opening and closing was simply realized with this parametrization and it also allowed to perform sweeping simulations at different gaps.

Another CST 3D Modeling feature is the chance to create or modify objects with transformations: section *Modeling*, menu *Tools*, action *Transform*; the available options are *Translate*, *Rotate*, *Scale* and *Mirror*. The advantage of this feature comes into play when, for instance, we need to deal with a symmetrical structure such as the TDI. Half of the moving parts, first of all the jaws, were created from their symmetrical half with the mirroring option. Since the moving parts were parametrized (the main parameter was *hgap*, for obvious reasons), a parameter update gave rise to the movement of both the original and the mirrored components.

A problem related to the Mirror option is that mirrored components are necessarily linked to the originals. The modifications on one of them affect also the other one, independently of user's preferences. It can sometimes be desirable to create a structure with the aid of Mirror just to avoid repeating the same creation steps twice (or more), and not because the components should always keep the symmetry after their creation. In order to allow this, the new checkbox *Indipendent* was recently introduced in CST, in the Mirror interface window. This checkbox was introduced in the last CST versions, but after the creation of the original model we worked on. Therefore, the components properties in our model could not be changed with the more recent *Independent* option. Some simulations had to be performed with asymmetrical jaw displacements and, instead of creating the model from the beginning, the alternative described in the following was adopted.

To obtain an independently moving-jaws model, about half of the jaws related components were only required to translate on the y axis, keeping motionless their mirrored ones. It was observed that the Mirror's symmetry plane coordinates, accessible from the Mirror interface window, could also be parametrized. The final parameters required for this model upgrade were *hgapT* for the top jaw displacement and *hgapB* for the bottom jaw displacement. We would like to point out that, despite of the parameters names adopted for inheritance from the symmetrical moving structure, hgapT and hgapB are not literally *half gaps* when the jaws are asymmetrically displaced.

With the graphical analysis of Figure 5.1 and Figure 5.2 the following was derived. Let's define the following parameters: hgapT as the top jaw displacement from the y = 0 plane, with the direction represented in the figures, hgapB as the bottom jaw displacement from the y = 0 plane, with the direction represented in the figures, y_s as the symmetry plane y coordinate (0, by CST default). Our goal was to determine the symmetry plane coordinate as a function of hgapT and hgapB in order to translate one jaw, leaving motionless the other one (as represented in Figure 5.2, for instance). Trivially, the distance between each jaw and

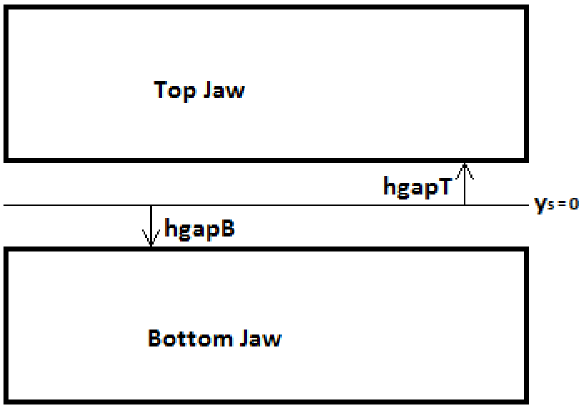

Figure 5.1: Two jaws representation to derive the symmetry plane coordinates for the single-jaw movement. In this picture, since hgapT = hgapB, the symmetry plane overlap the origin plane, hence $y_s = 0$.

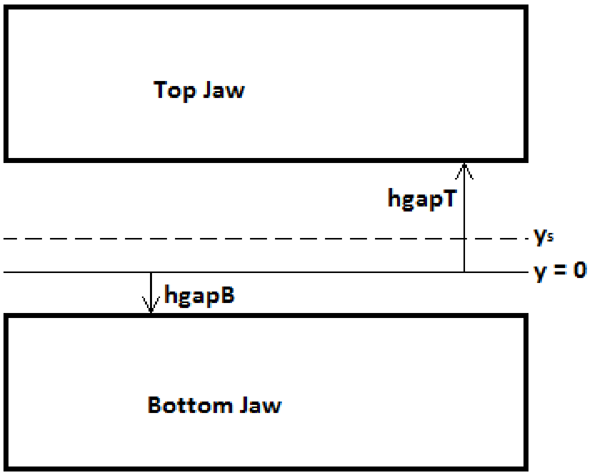

Figure 5.2: Two jaws representation to derive the symmetry plane coordinates for the single-jaw movement. In this picture, since hgapT $>$ hgapB, the symmetry plane (dashed line) is above the the origin plane (solid line), hence $y_s > 0$.

the symmetry plane is half of the jaws' separation distance (left term of (5.6)). This value also corresponds to hgapB summed to the symmetry plane y coordinate (right term of (5.6)). Then, we could easily derive y_s:

$$\frac{hgapT + hgapB}{2} = hgapB + y_s. \tag{5.6}$$

$$y_s = \frac{hgapT - hgapB}{2}. \tag{5.7}$$

Once we obtained this result, the symmetry plane y coordinate was modified in the History

List entries related to mirrored components. In spite of this, the solution described above did not suite components that, when the gap changed, underwent movements more complicated than a simple y translation. Two groups of elements belonged to this category: the ones that in the TDI 3D model were named *foils* and *supports*, because they where rotating and changing shape depending on the associated jaw's displacement.

To deal with this components, reverse engineering from History List was required, using also the final components' properties. Then the originals were kept, whereas the mirrored objects were deleted and manually created step by step. In Figure 5.3, a caption of one of the steps for a bottom foil creation is reported, close to the final result.

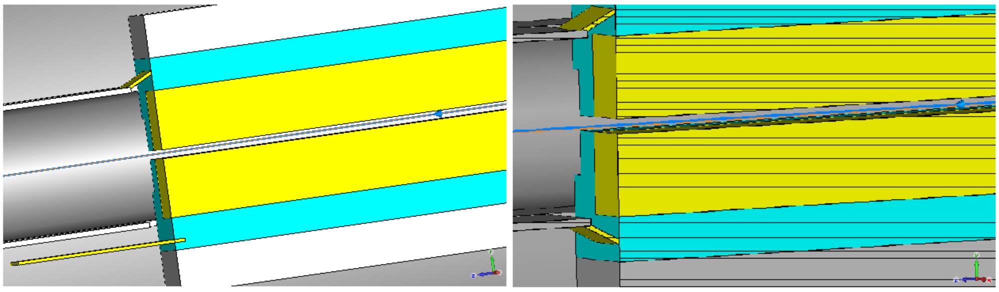

Figure 5.3: Intermediate step (left) and final result (right) for one of the bottom foils manual creation, following the History List steps of the correspondent top one, also visible in both the captions.

5.3 Comparisons between segmented and not segmented model and between symmetrically and asymmetrically positioned jaws

The updated model that allowed the independent jaws movements was used for the *Wake solver* simulations that will be discussed in the following. Before dealing with these simulations, some remarks on the TDI 3D model and simulations will be given.

As we said before, CST takes into account the geometry contributions to impedance, linked to peaks that are often easily visible in the impedance curves. On the other hand, CST cannot realistically estimate the wall part of the impedance, especially when there are elements very close to the beam, such as the jaws at working position. One of the main reasons of this is that the actual coating was three order of magnitude thinner than the other components and they could hardly be simulated together in CST. The absorbers blocks were eventually modeled only with the first material exposed to the beam (copper). The approximation holds better for higher frequency, when the fields penetrations in the surrounding equipment becomes smaller (the well known skin effect).

According to what we just explained, the tune shift values that will be derived from CST simulations should mainly be considered for comparisons with other CST simulations' ones, such as between the segmented and not segmented TDI model, and they should not be singularly used as a numerically correct estimation of what we would obtain in the machine.

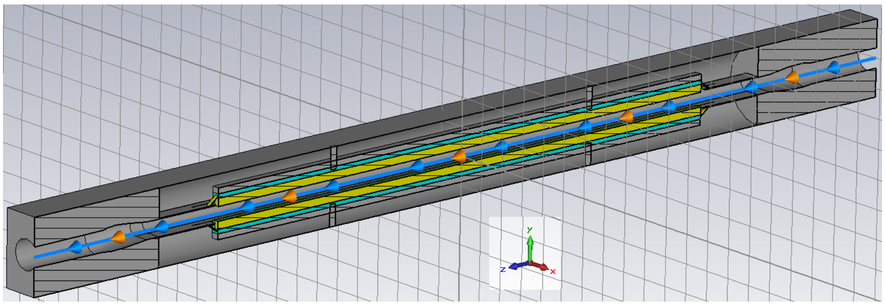

Figure 5.4: TDI simplified model and coordinate system. Vertical plane section.

Jaws' segmentation (Figure 5.5, used in occasion of the TDIS Meeting [25], and Figure 5.6) is a recent model upgrade made by B. Salvant, accordingly to the real TDI. This model upgrade was related to the fact that we wanted to investigate the relevance of the TDI geometry on its impedance, and these segmentations could give, as one might expect, a considerable contribution to it.

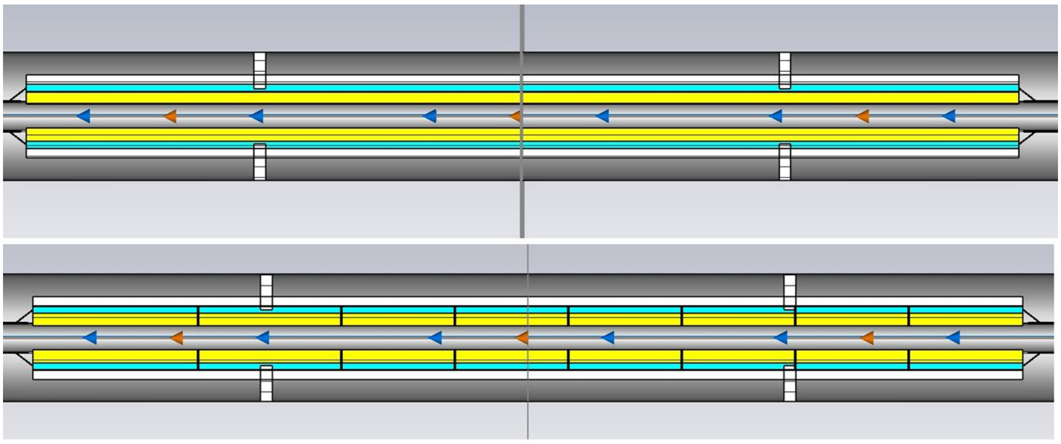

Figure 5.5: Vertical plane (xz) sections comparison between not-segmented TDI (top) and segmented TDI (bottom).

In Figure 5.7, Im$[Z_y]$ is compared for segmented (blue curve) and not segmented (red curve) TDI. Figure 5.8 shows a detail. The choice to report Im$[Z_y]$ was made because, as we saw in section 2.3, it has a large impact on the tune shift. The y axis is normalized for 1 mm axis

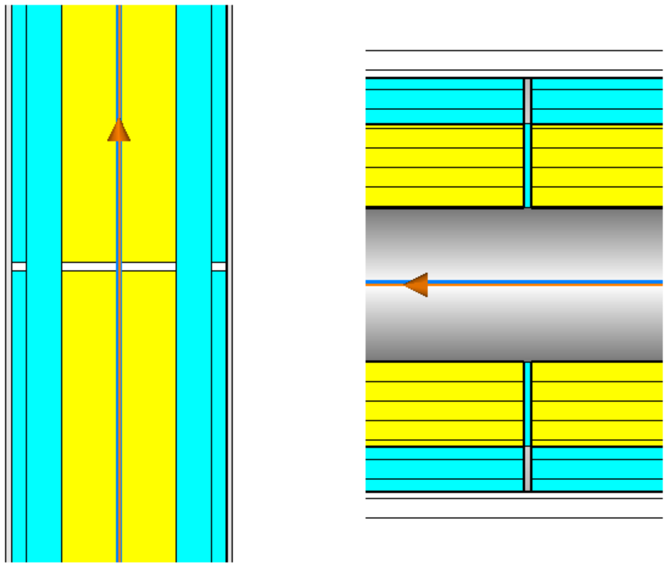

Figure 5.6: Detail of the segmented TDI horizontal plane (xz) section (left) and vertical plane (xz) section (right).

displacement and values were therefore multiplied for a scale factor of 1000, before being used for further calculations.

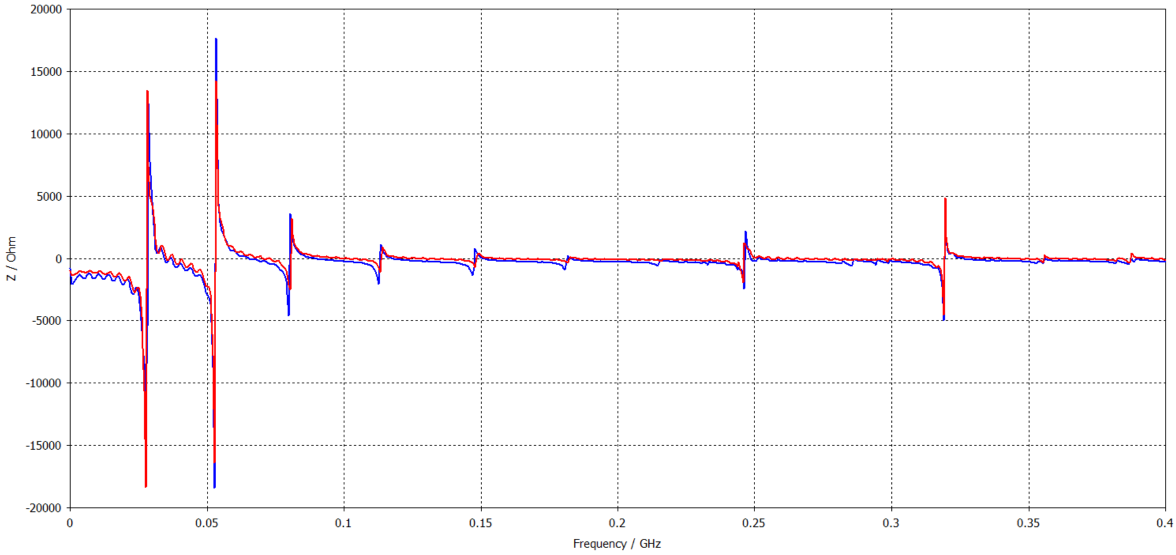

Figure 5.7: Im[Z_y] for segmented TDI (blue) and not segmented TDI (red).

Despite the fact that the difference between the two curves looks relatively small, this difference affects the shift quite considerably. MatLab derived Vertical tune shift values are reported in Table 5.1 and Table 5.2 for TDI2 and TDI8, respectively. TDI2 and TDI8 refer to the same CST model but they gave different tune shifts because of their different β_y. Values for asymmetrically positioned jaws are also reported in the same tables (asymmetrical positions with respect to the beam: hgapT = 2.5 mm and hgapB = 50 mm).

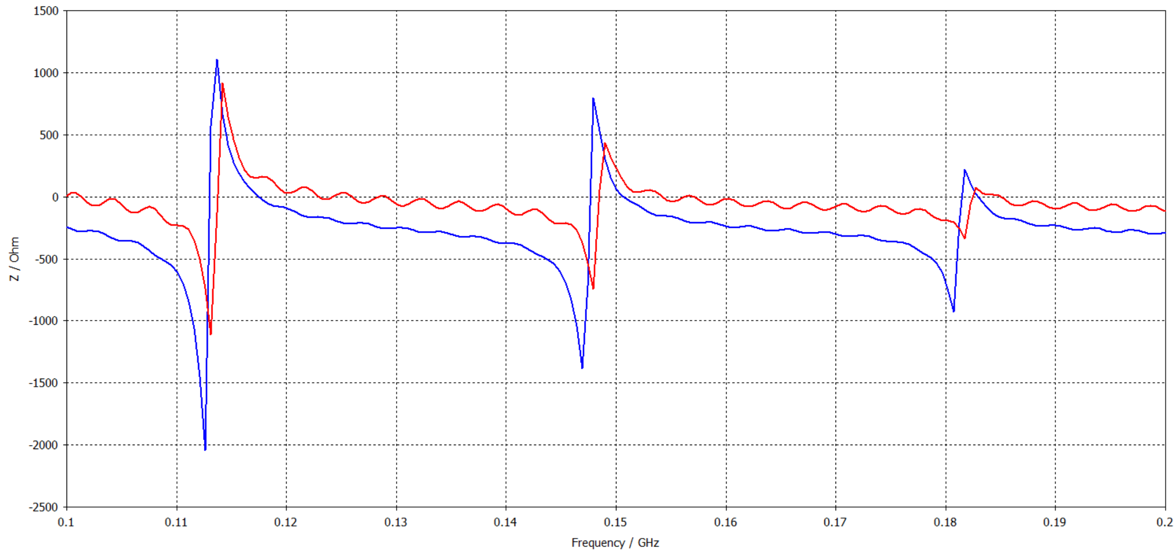

Figure 5.8: Im[Z_y] for segmented TDI (blue) and not segmented TDI (red). Zoom of Figure 5.7.

	Not segmented	Segmented
$hgapT = 2.5\ mm$ & $hgapB = 2.5\ mm$	1.6×10^{-5}	4.2×10^{-5}
$hgapT = 2.5\ mm$ & $hgapB = 50\ mm$	2.0×10^{-5}	6.5×10^{-5}

Table 5.1: TDI2 Vertical tune shift calculated from CST simulations results.

	Not segmented	Segmented
$hgapT = 2.5\ mm$ & $hgapB = 2.5\ mm$	1.4×10^{-5}	3.8×10^{-5}
$hgapT = 2.5\ mm$ & $hgapB = 50\ mm$	1.8×10^{-5}	6.0×10^{-5}

Table 5.2: TDI8 Vertical tune shift calculated from CST simulations results.

If the geometry gave a negligible contribution, we would have had impedance about twice when both the jaws are close to the beam, compared to the single-closed-jaw case. In other words, the resistive wall contribution should be dominant, and it should double when both jaw are closed. Our tune shift results, instead of being smaller, are larger for the single-closed-jaw case.

Thus, we can conclude that the geometry has a deep relevance in TDI simulations: IW2D numerical simulations simply do not show us the full picture. The segmentation update of the model led to a factor around 2.5 on shift at symmetrically closed jaws. This factor, together with possible measurement errors, justified the remaining mismatch between expected results and MD measurements (we are referring to the contour plots seen in section 4.3). Considering the model's simplifications, intrinsic measurement and data elaboration errors, we could therefore have a good confidence on the TDI - Graphite's coating good conditions at the present run. Furthermore, the fact that the TDI's tune shift was about one order of magnitude lower than last year and that the phase shift was so small that it was practically not measurable, allowed the team to have more confidence in the decision making process related to the design of the TDIS, the TDI future replacement for HL-LHC.

5.4 Vacuum spikes investigation

As time passed by from the start of LHC run 2016, the energy and the number of bunches in the LHC were increased. Starting from the end of May, vacuum spikes have been observed when retracting the jaws from the working position to the parking one. These spikes (see, for instance, Figure 5.9) are sharp vacuum degradations, like the ones that can be caused by an undesired flux of particles. In the previous injections at lower energies vacuum variations were already observed while retracting the jaws. However, those variations were expected and not dangerous, basically given by the system mechanical movement.

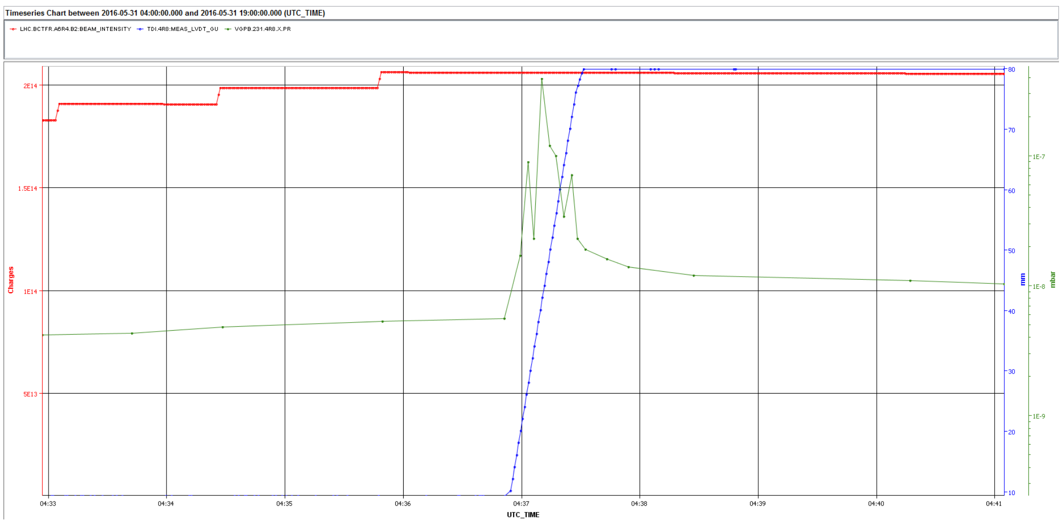

Figure 5.9: TDI8 vacuum spike (green). On the same temporal scale, TDI8 full gap (blue) and Beam 2 intensity (red).

The importance of the 31 May case (and also of the following ones) was due to different factors: it happened only for TDI8, during retraction, at hgap between 20 and 30 mm, for high intensities, the vacuum recovery that was supposed to follow was slower than it should and sometimes absent. This last factor sometimes led to the beam dumping.

Despite the retraction to the full parking position was not strictly necessary to operate the LHC at its full regime, the lack of full understanding of what was exactly happening in the machine required further investigations. The main hypothesis to justify the spikes was that some of the TDI components were outgassing when exposed to heavy thermal stress at the retraction.

Since the TDI structure geometrically change during the retraction, also its resonant modes change accordingly. These shifts were analyzed with CST, performing hgap-sweeping simulations. The collected data were then processed with MatLab to obtain the contour representation of Figure 5.10. The red dashed lines stand for the beam frequency lines, because of the 25 ns bunch spacing. The discontinuities of the colored areas are caused by the finite number of the simulations, made varying the hgap between 15 and 30 mm. The chosen step was 0.5 mm and it was considered sufficient to see the resonance shifting trend.

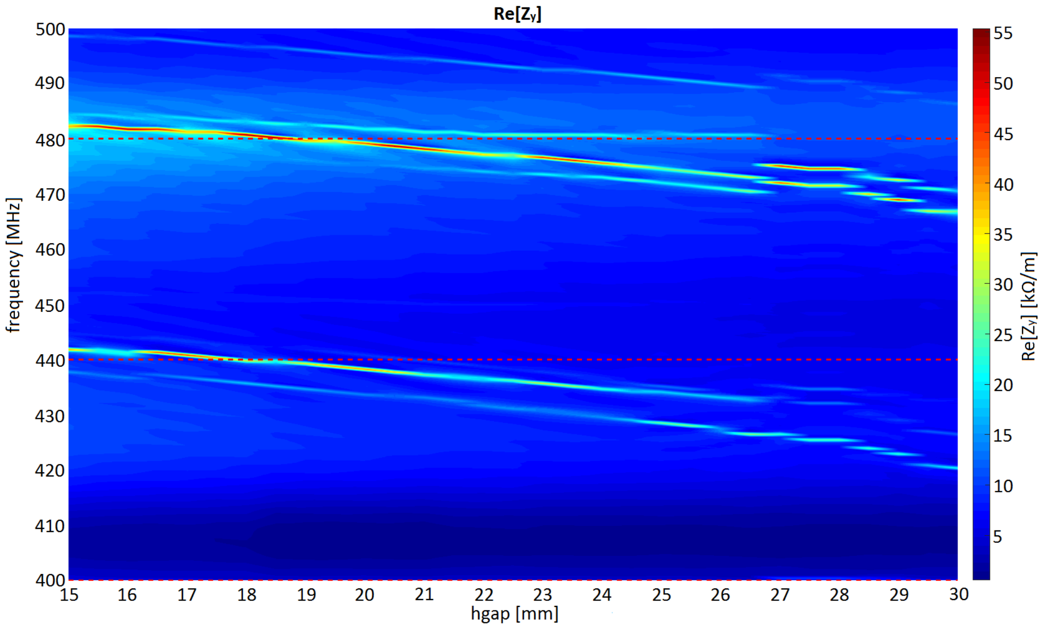

Figure 5.10: TDI resonant modes when varying the gap, from CST wakefield simulations. The hgap critical values are the ones that meet the largest $\mathrm{Re}[Z_y]$ at the beam's spectral lines (that is at the red dashed lines).

At some points during the retraction, the structure showed resonant modes that the beam could excite, that is where the dashed lines meet the high impedance areas. Nonetheless, the TDI is a massive device and the modes excitation may need time intervals in the order of seconds. Moreover, the jaws heating can require minutes. The jaws retraction speed was therefore needed to complete the study, understanding how much time the TDI usually spent in the one that we addressed as critical positions.

Again with the aid of MatLab, Timber data for a TDI typical retraction have been represented on the plot of Figure 5.11.

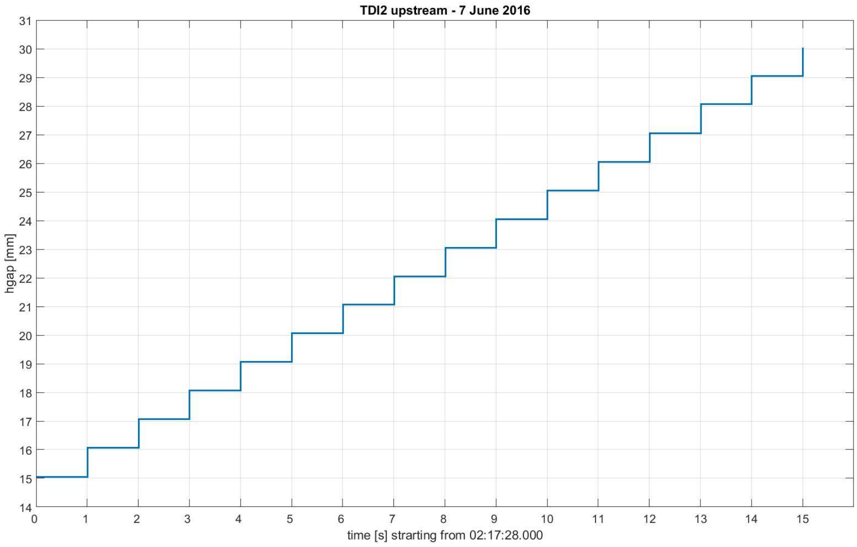

Figure 5.11: Times for a typical retraction as a function of time. The example shows TDI Upstream Gap on 7 June 2016, at 02:17:28.

As it can be easily verified, the retraction speed of each jaw can be estimated as $\Delta hgap/\Delta t \approx 1\ mm/s$. Accordingly to this data, it should be possible to predict the thermal capacity of a component that could have been through a strong thermal stress and, eventually, outgassed. From this estimation, the range of TDI components could be then restricted to select a possible responsible for the spikes.

Chapter 6

CST simulations of the TDIS for HL-LHC

In the present chapter we will firstly introduce the HL-LHC project and the TDIS. The TDIS was still in its designing stage and some parameters have been studied from different points of view. Our interest lied in some of these parameters, such as the modules spacing, the *fingers* configuration and the absorbers material, which will be discussed in detail later in this chapter. The simulations we carried out investigated the combinations of these parameters' possible values or configurations.

Going more into details, in the following sections we will firstly observe the peaks behavior of the longitudinal impedance real part while changing the modules spacing.

Afterwards, we will check the impact of three different fingers configurations on the tune, together with the tune's trend when changing the modules spacing.

We will then use the impact on the tune to compare two different absorbers materials: graphite and copper. Concerning this, the TDIS CST model, as the TDI one, had no coating modeled on the absorbing blocks, which were entirely modeled with the closest material to the beam. So, when investigating the impact of the copper coating on the graphite absorbers, we actually compared the results of two models where the absorbers were modeled either with graphite or with copper. Some impedance plots will be reported in order to discuss some problem we faced using graphite as the absorbers material.

The tune shift we will provide for each combination in this chapter was computed starting from CST simulations, that consider the structure geometry but that may incorrectly estimate the wall impedance contribution. As we already discussed once in the previous chapter, it is worth to stress that the tune values obtained in this way should mainly be used for

comparisons with others derived from CST as well in order to investigate the parameters impacts, and not directly as a tune realistic estimation.
Nevertheless, using caution and complementing the analysis with the IW2D wall impedance contribution (courtesy of David Amorim, CERN - BE department), we will observe when the geometry gave a contribution to impedance much larger than the wall factor. In that case some comparison with the *LHC impedance model* were carried out, highlighting the only case where the simulated impedance exceeded the LHC one: the dipolar impedance real part at injection (that is at hgap = 3.8 mm).
A machine's *impedance model* is the overall impedance contribution of its component. In this case, we used the LHC model without the TDI, since it gave one of the largest contribution to it and it was supposed to be replaced with the TDIS.
In the last comparisons we used the LHC impedance model instead of the HL-LHC one because more studies were performed on the former, being the latter on the way of definition.
Most of the pictures, plots and considerations we will provide in the present chapter were used at the second Impedance Working Group meeting [31].

6.1 TDIS for HL-LHC

The LHC nominal Luminosity of 10^{34} $cm^{-2}s^{-1}$ was recently achieved, on 10 July 2016. However, a major upgrade to increase the target Luminosity and called *High Luminosity-LHC* (*Hi Lumi*-LHC, or simply HL-LHC) was already scheduled [32]. Practically, the upgrade consists in the substitution of several components during the *Long Shutdown* 2018/19. The new Luminosity target will be reached mainly thanks to the upgrade of the triplets region, that will further decrease the beam size before the collision.
Our interest focused on the TDIS (i.e. the *Segmented TDI*), that will replace the TDI. Its simplified 3D model that was used for the CST simulations is depicted in Figure 6.1. Due to the higher Luminosity in the HL-LHC, the constraints on the TDIS are different from the one on the TDI. Some preliminary considerations on material and design are reported in [33].
In the next sections we will investigate same variations on the design and the materials in terms of impedance and tune shift, with the aid of CST simulations. The longitudinal segmentation in three modules (i.e. the origin of *Segmentation* in TDIS) and the *fingers* placed between them are two main differences from the TDI and they will have a fundamental role in the simulations comparisons.
The reasons that led to the TDIS segmentation in three separate modules are mainly

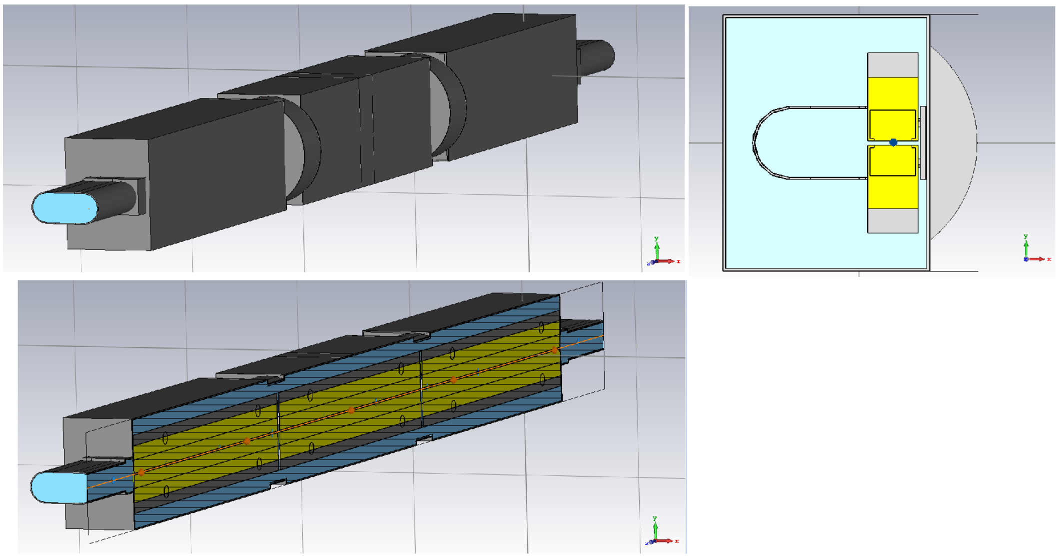

Figure 6.1: TDIS simplified 3D model for CST simulations. On the top-right its section on the xy plane (perpendicular to the beam's direction). On the bottom left its vertical plane section. Differently from the TDI, the jaws are not in the geometrical center of the structure. Consequently the beam's path is not at $(x_S;\ y_S) = (0\ \text{mm};\ 0\ \text{mm})$, but $(x_S;\ y_S) = (59\ \text{mm};\ 0\ \text{mm})$. Thus, in this case when we refer to the vertical plane we mean the one at x = 59 mm.

mechanical and thermal. Indeed, it will allow independent (therefore easier installation), replacement and movement control for each module. Furthermore, the dilatation induced by the thermal stress will give less boundaries and less chance to tilt or deform the structure.
As we did for the TDI CST model, also the TDIS one was firstly updated to allow the jaws independent translation on the y axis, using the same technique we described in section 5.2. Again we faced some problems with a few components, but they were handled with History List's entries manipulations.

6.2 Modules spacing impact on the impedance peaks

One of the biggest differences between TDI and TDIS, which can be easily appreciated already in the simplified 3D model, is its division in three modules along the longitudinal axis. These modules are mechanically independent, but some software boundaries will avoid large gap differences between adjacent modules. This boundaries are also needed to avoid the damaging of the *fingers*, that we will present in the following section.
In this paragraph we report sweep simulations of the parameter we called *newgap*, that is the longitudinal spacing between adjacent modules. The other parameters that will

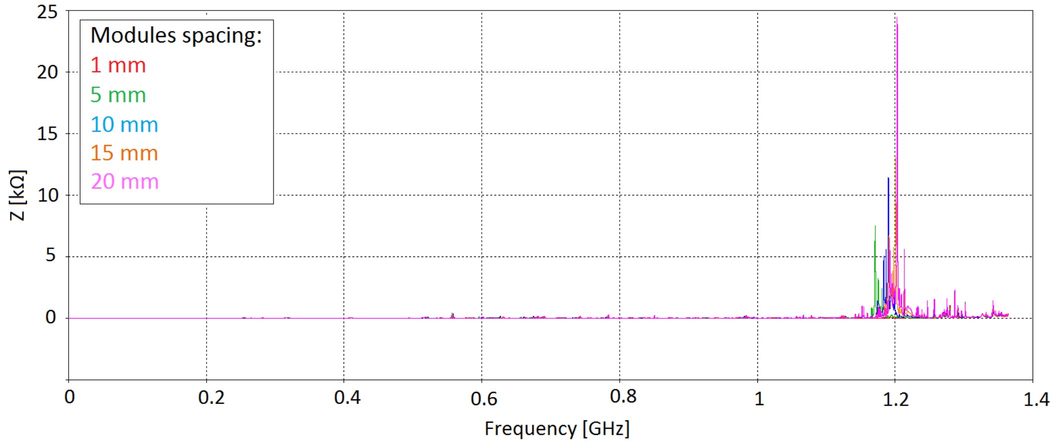

Figure 6.2: Re[Z_l] with maximum number of DFT points (about 800000 in this case). Different curves' colors correspond to different newgap values. Details of this plot are reported in Figure 6.3 and Figure 6.4.

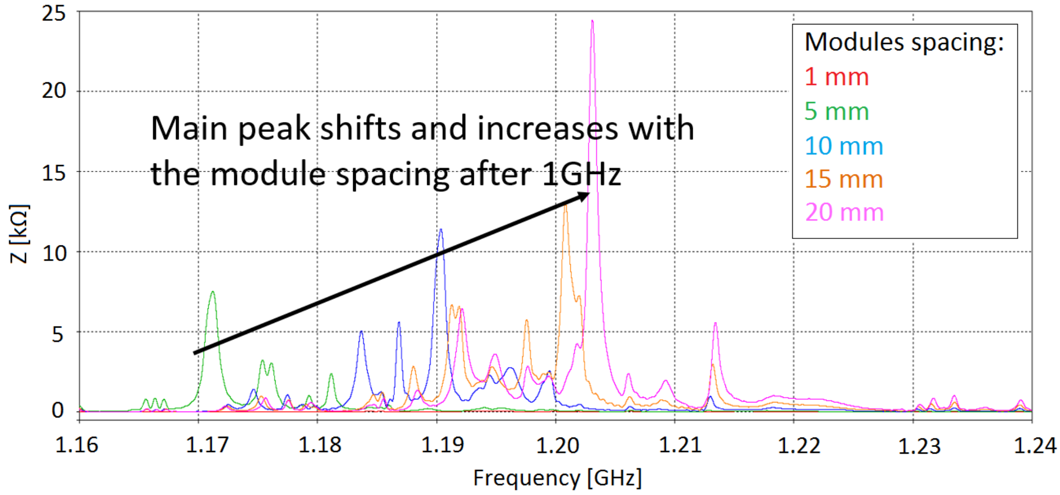

Figure 6.3: Detail of Figure 6.2 close to its highest peak, around 1.2 GHz. Different curves' colors correspond to different newgap values. Apart from the red curve (newgap = 1 mm), which is almost flat compared to the others, the main peak's amplitude grows with the newgap. Similarly, it also shifts to higher frequencies.

be investigated in the following sections were fixed: hgap = 3.8 mm, copper absorbers, no fingers between the modules. When increasing the newgap, the modules' length was decreased proportionally, in order to leave the TDIS total length unchanged. Since the TDIS is still at its designing stage, some of its characteristics are not permanently established yet, and alternatives are investigated to find the best compromise from different points of view: mechanical, thermal, beam's stability, vacuum and others. The newgap is an example of parameter that can still variate and we wanted to see its impact on impedance and tune shift. Since the spacing between the modules is a relevant discontinuity on the beam path, one

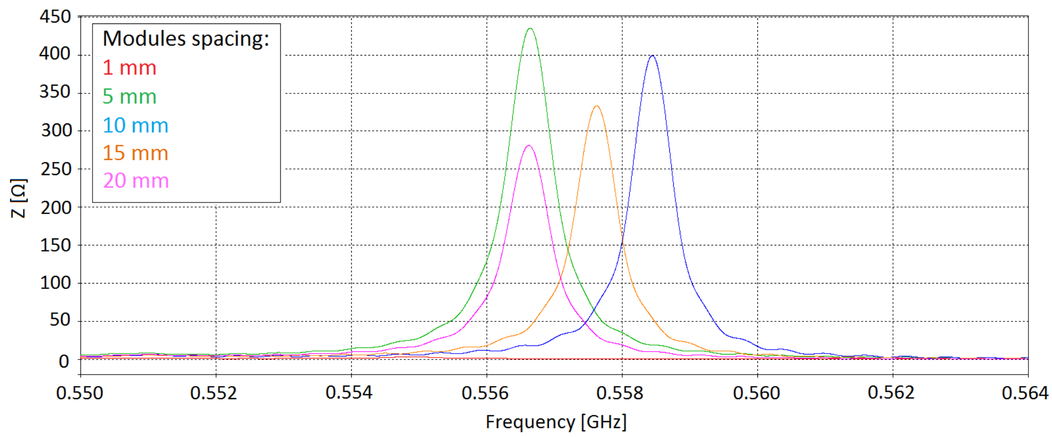

Figure 6.4: Detail of Figure 6.2 around 0.557 GHz. Different curves' color correspond to different newgap values. The curves' smoothness achieved with the large number of DFT points gave us more confidence on the amplitude values' effectiveness.

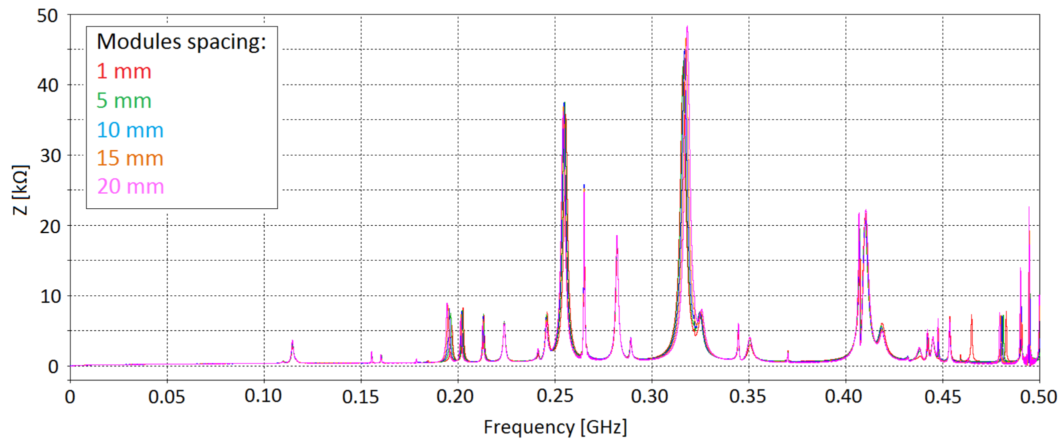

Figure 6.5: Detail of Figure 6.2 between 0 GHz and 0.5 GHz, that is where the highest part of the LHC bunch's spectrum lies. Different curves' color correspond to different newgap values. The impedance values are lower by far than the ones of the rest of the spectrum. The curves, including the one for newgap = 1 mm, are practically overlapping.

can expect that increasing the newgap leads to a larger impact on impedance. Nevertheless, this relation between amplitude and newgap changes depending on the frequency range we observe.

- For frequencies higher than 1 GHz (Figure 6.3) we can observe the amplitude growth and the frequency shift of the main peak, when increasing the newgap.

- Between 0 and 0.5 GHz (Figure 6.5), the impedance curves are practically overlapping, including the one for newgap = 1 mm. In this interval, impedance was much lower than in the rest of the analyzed spectrum, nonetheless it is also the range where the most of an LHC bunch's spectrum lies.

- In the intermediate frequency range (i.e. approximately between 0.5 and 1 GHz) we had a mixed behaviour: some peaks stayed constant, some others increased or decreased in amplitude, combining it with frequency shifts.

These simulations were performed with the largest possible number of DFT points, larger than 800000 in this case, to be able to investigate the peaks in details. The curves smoothness, also when zooming on the sharpest peaks, is a confirmation of the peaks' representation reliability (see, for instance, Figure 6.3 and Figure 6.4).
The vertical tune shift (Table B.1) was computed with MatLab and it grows with the newgap, showing a saturation for larger module spacings. It will be discussed in the next paragraphs, in relation with fingers configurations and absorbers materials.

6.3 Fingers impact on the tune shift

TDIS modules are in contact with each other through flexible conductive material elements called *fingers*. Their task is to shield the beam, letting it experience as more conductive surface as possible. In other words, these fingers are a barrier for wakefields, but at the same time they are flexible enough to allow separately moving modules and their separate installation in the machine.
The way this fingers were modeled and the position where they were placed obviously affected the simulations and, consequently, impedance and tune shift. The following results come from simulations where we considered two possible fingers placements with the simplest modeling, beside their absence. They could not be placed too close to the beam, otherwise they would not stand the thermal stress, but the closest they are the larger their effect is expected to be.
In the previous paragraph's simulations the fingers were simply modeled as bricks, touching both the modules between which they were placed. The bricks *material* was vacuum, so they did not affect the results. We repeated the simulations changing the bricks material from vacuum to *Copper (annealed)* (from CST library, the same used for absorbers and other TDIS components representation in the 3D model). The three different fingers configurations will be addressed in the following as *no fingers*, *far fingers* and *close fingers* (see Figure 6.6). The first one, is the one used in the previous paragraph.

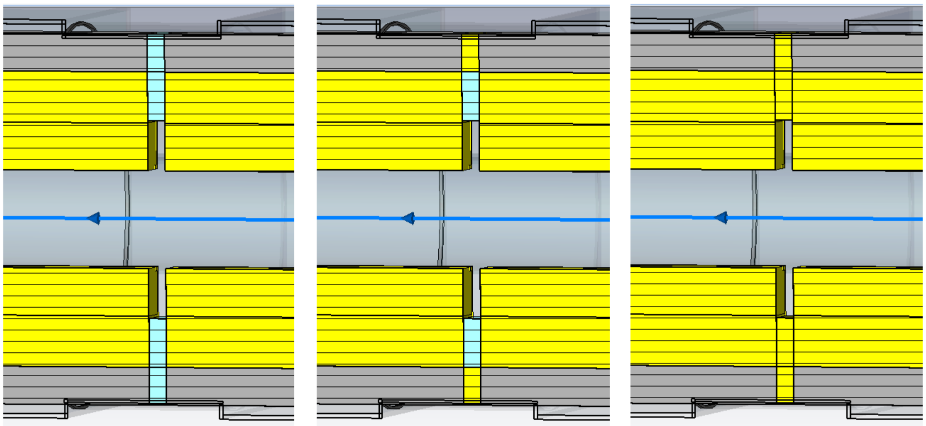

Figure 6.6: The three different fingers configurations in the CST simplified 3D model of the TDSI, represented in the vertical plane cross-section: *no fingers* (left), *far fingers* (center), *close fingers* (right).

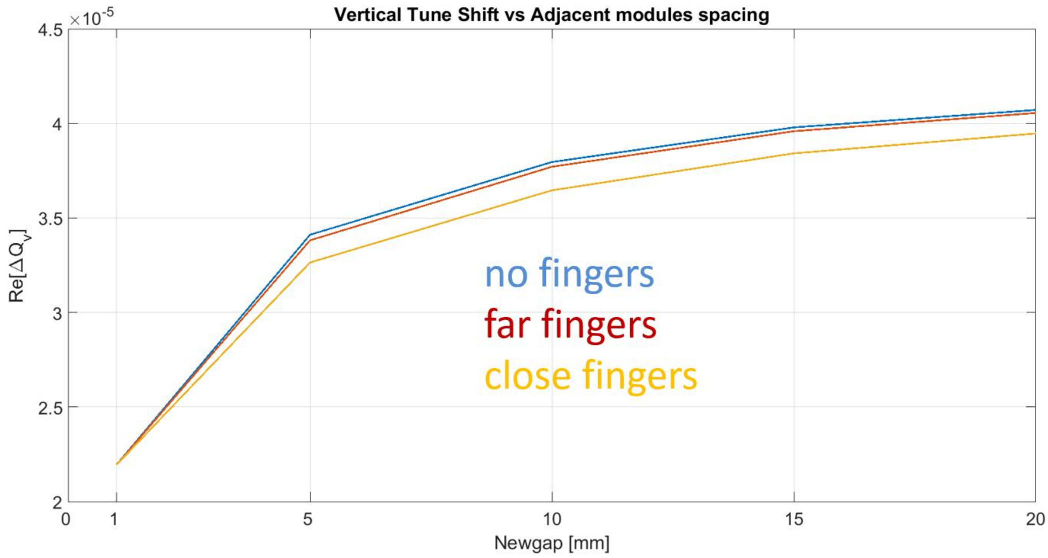

Figure 6.7: Tune shift as a function of the modules' spacing. The curves are parametrized on the different fingers configurations for closed jaws and copper absorbers.

In the plot of Figure 6.7 the three different fingers configurations are compared at injection for copper absorbers and different newgap values. The main highlight is that the fingers gave a positive contribution, as expected, and that this contribution grew bigger with larger newgaps. The best contribution (i.e. the smallest tune) was obtained for the close fingers configuration. The worst one was given by the fingers absence whereas the far fingers configuration gave an intermediate situation, very close to the no fingers one.

The other point we should focus on is that the tune shift exhibited saturation with the increasing modules spacing, approximately around newgap = 10 mm.

Repeating with graphite absorbers instead of copper we had larger tune absolute values, but

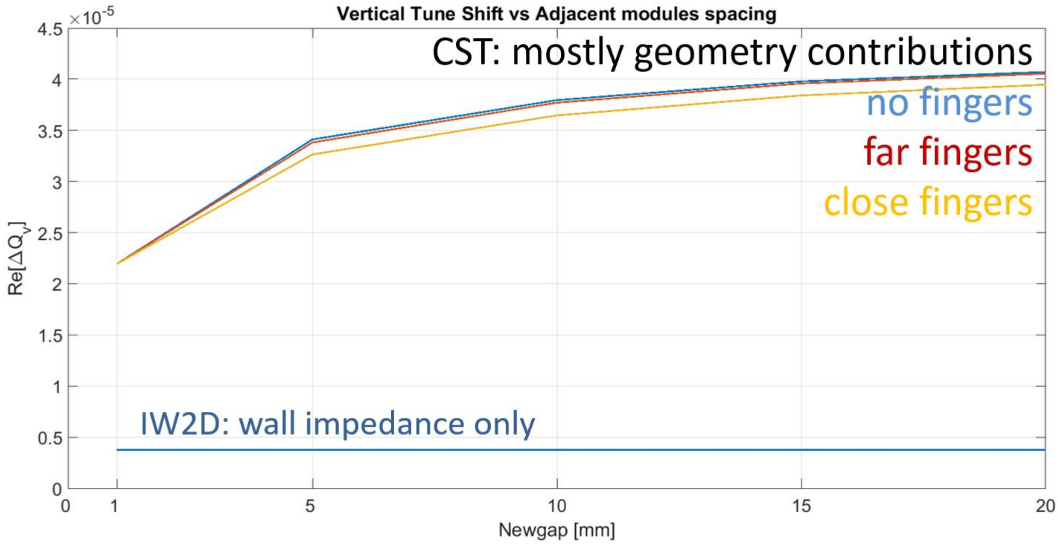

Figure 6.8: Tune shift as a function of the modules' spacing for a single bunch with 9 cm bunchlength and N = 1.15×10^{11}. The curves are parametrized on the different fingers configurations for closed jaws and copper absorbers. The curves in the bottom represent the tune shift computed starting from IW2D results, where the same structure adopted in CST was used to model a Flat Geometry.

the relations between the curves and the conclusions stayed the same.

Superimposing the tune obtained from the IW2D-computed wall impedance for the same layers structure of the CST model (53.5 mm copper absorbers and 57.5 mm copper supports on both the beam's sides), we drew the conclusion that for copper absorbers, at injection, most of the tune is given by the geometry (see Figure 6.8) and both the CST derived impedance and tune could be used for further comparisons. As we will see in the next paragraph this was not the case for the graphite absorbers. The IW2D curve is constant because in its code we modeled the structure as a Flat Geometry as long as the whole jaw, without discontinuities.

6.4 Absorbers material impact on the tune shift

Beside the three different fingers configurations, the simulations were also repeated changing the absorbers material from *Copper (annealed)* (CST library, $\sigma = 5.8\times10^{7}$ S/m) to graphite (σ = 66666 S/m), and at flattop (hgap = 55 mm) instead of injection (hgap = 3.8 mm). Considering the newgap sweep, fingers configurations, absorbers material, hgap, both dipolar transverse impedance and longitudinal impedance simulations, the total amount of simulations raised to 120. They were run on the HPC CERN cluster [34], which provides machines with 16 cores and 128 GB of RAM for technical software simulations. Beside its documentation, a more detailed user guide, including also occurred errors and shortcuts, was drafted as a reference for the other CST users at CERN and presented at one of the Impedance Meeting [35].

The tune shift for all the cases given by the 60 (transverse impedance) combinations is reported in Appendix B. In the present section, as in the previous, some considerations on those data will be made with the aid of plots.

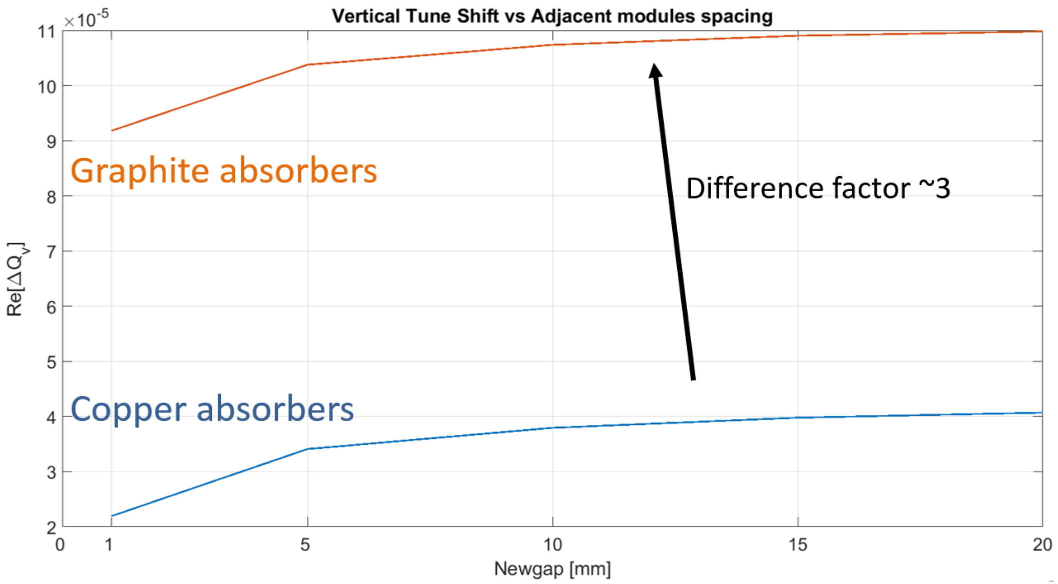

Figure 6.9: Tune shift as a function of the modules' spacing for a single bunch with 9 cm bunchlength and N = 1.15×10^{11}. Both the absorbers material (copper and graphite) are represented at injection, with no fingers.

In Figure 6.9's plot, two different absorbers materials are compared at injection with no fingers. The graphite led to an increasing factor 3 in the tune, compared to the copper curve. The conductivity of graphite we used in CST is about 3 order of magnitude lower than the copper one, so an increment in terms of impedance and tune was expected.

As in the previous paragraph, we again superimposed IW2D wall impedance's contribution to the tune (Figure 6.10). Whereas for copper absorbers the geometry gave the largest contribution to the tune, graphite showed approximately the same contributions from both CST simulations results and IW2D ones, probably due to the lower conductivity.

The high slope at low frequency in the transverse impedance imaginary part for all the different newgaps (Figure 6.11) was also visible in the IW2D transverse impedance. This pointed out that probably a considerable contribution to impedance was taken into account in both CST and IW2D: summing the two would still give a worst case, but it may also

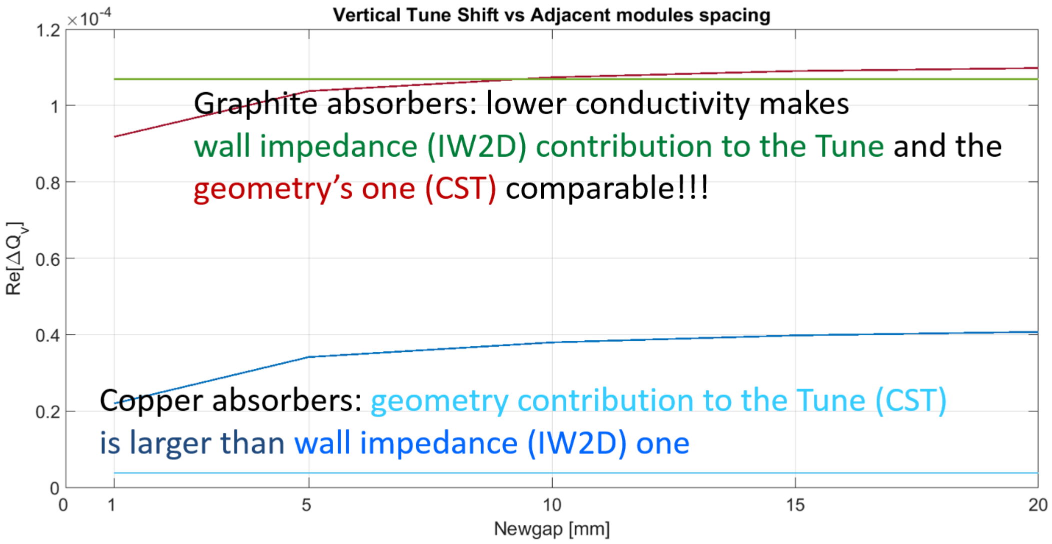

Figure 6.10: Tune shift as a function of the modules' spacing for a single bunch with 9 cm bunchlength and N = 1.15×10^{11}. Both the absorbers material (copper and graphite) are represented at injection, with no fingers. Two separate curves are drawn for the tune shift computed starting from IW2D simulations, where the same structure adopted in CST was used to model a Flat Geometry.

overestimate it.

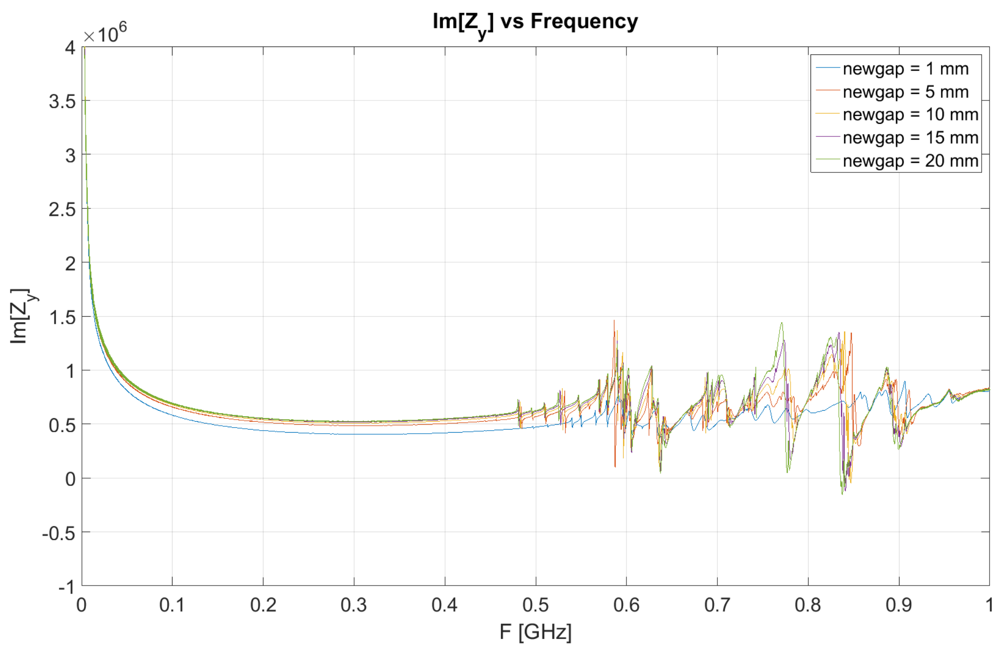

Figure 6.11: Transverse impedance imaginary part from CST results, for different modules spacings, at injection, with no fingers and graphite absorbers.

Repeating with open jaws (i.e. at flattop) we had tune values smaller by 3 orders of magnitude compared to injection, and the relations between the curves and the conclusions were almost the same. The saturation that we appreciated in the plots for closed jaws, was less pronounced when the jaws were open. The close fingers configuration was again the one with the smallest tune contribution and again copper as absorbers material led to smaller tune than graphite.

All the values for the parking position, as can be checked in Table B.3 and Table B.4, would be too small to be measurable in the machine, and they would practically let the TDIS be transparent to the beam. Of course, as we discussed, absolute values from CST should be treated with caution. However, the crosscheck we did with IW2D allowed us to consider the sum of their contributions as a worst case and, also taking this into account, the flattop values would still stay far below the measurability, which is set to 1×10^{-5}.

6.5 Comparisons with the LHC impedance model

In this section we will show two comparisons between the impedance we estimated in CST, the IW2D impedance computed by D. Amorim and the LHC impedance model. The CST results used for these comparisons where the ones at newgap = 10 mm and with no fingers.

For almost all the impedance components we calculated (real and imaginary part of both vertical dipolar and longitudinal impedance, at injection and at flattop) the LHC impedance model without TDI was considerably larger than the simulated curves.

The situation where our results and the LHC model approached the most was the one of the dipolar impedance at injection, as shown in Figure 6.12. An amount of impedance this large gave us an important warning, since it can lead to considerable contributions on the overall machine impedance, affecting tune shift and instabilities rise times. Further investigations will be carried out starting from these results.

In the imaginary part (right hand plot in Figure 6.12) we can appreciate what we stated above: the graphite slope at low frequency is present in both CST and IW2D results, letting us suppose that a large contribution was considered in both the software and explaining at least partially the comparable tune shift curves for graphite absorbers (Figure 6.10).

6.6 Conclusions

To summarize what achieved in this chapter, we investigated the impedance behaviour for different modules spacing, concluding that the higher the frequency the more the peaks were affected by the spacing. The strongest resonances were observed close to 1.2 GHz.

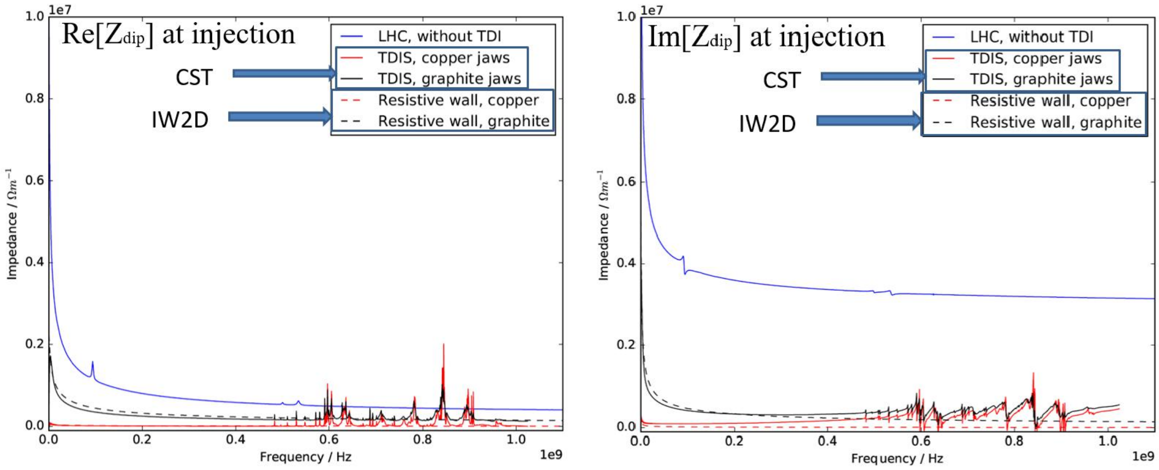

Figure 6.12: Dipolar impedance real part (left) and imaginary part (right) at injection. The CST curves were obtained from simulations with no fingers at newgap = 10 mm. As for the IW2D curves, the Flat Geometry had the same symmetrical structure of the respective CST simulation. On both the beam's sides there were, starting from the closest: 53.5 mm of copper for the absorbers and 57.5 mm of copper for the support (red dashed lines), or 53.5 mm of graphite for the absorbers and 57.5 mm of copper for the support (black dashed lines).

The tune shift exhibited saturation for module spacing larger than 10 mm, approximately, and the fingers gave a slight decrement to it.

Modeling the absorbers with graphite instead of copper gave approximately 3 times more tune shift. Results worst than the copper ones were expected due to the 3 orders of magnitude difference between the materials' conductivities. Crosschecking with IW2D, we realized that the graphite CST simulations might have considered also a large part of the wall impedance, whereas for the copper the geometry gave the dominant contribution.

Further refinement of this studies can be carried out exploring alternative ways to model the coating in CST (such as *Thin Panel*, as suggested by the CST support) or computing and comparing also the vertical quadrupolar component of the transverse impedance, which is expected to be much smaller than the dipolar we already analyzed.

At last but not least, we showed which among our simulated impedance components approached the most the LHC impedance model without TDI, highlighting the need of further studies on the transverse impedance at injection.

Chapter 7

Conclusions

At the beginning of this thesis we presented CERN, the LHC and gave some concepts on particle accelerators and beams physics. We mainly introduced the wakefields, beam coupling impedance and tune shift, which followed us until the last chapters.

Following that, we started to discuss about the TDI, the *Injection Protection Collimator* of the LHC. We reported procedure and results of the measurements on the hBN blocks that were installed in the machine during LHC run 2015. Comparisons with wire measurements, complemented by IW2D simulations, let us conclude that the bad performance during run 2015 were mainly related to the degradation of the blocks' titanium coating, followed by the hBN exposure to the beam.

Before run 2016, the blocks were replaced with graphite, copper-coated ones, that showed much better performances, as we checked from the MD's data. However, this improvement was not as large as initially expected. After some other IW2D simulations and data manipulations we supposed that a good reason for the discrepancy was that IW2D was not considering the full TDI geometry.

CST was then introduced and helped us to confirm our hypothesis. Firstly, we updated the model to allow asymmetrical jaws displacement and we later verified our suppositions on the TDI geometry relevance. In the same chapter, we also used CST to investigate the vacuum spikes that were observed in the TDI presently installed in the machine: these results might help to find a range of possible components that could outgas, causing the spikes.

CST was eventually used to study the TDIS, that is the TDI upgrade for HL-LHC, still at its designing stage. We checked the impact on impedance and tune of different parameters combinations: modules spacing, absorbers material and fingers configuration. We observed the impedance peaks behavior with the modules spacing changing with the observed frequency range. We pointed that the tune showed saturation when increasing the modules spacing and that the fingers gave a reduction. Graphite absorbers gave tune approximately 3 times larger than copper absorbers. However, since in the graphite case impedance from CST and IW2D was very similar in a large frequency interval, we supposed that CST considered also a large part of the wall impedance, letting the tune computed from both the software be very similar.

Finally, we compared some of our results with the LHC model, highlighting where they were comparable to it, that is in the dipolar impedance at injection. Beside the considerations we made, further analysis will be carried out aiming to improve the reliability of the simulations involving graphite, to benchmark the impedance peaks with other types of simulations (such as CST's *Eigenmode* Solver) and to permanent establish the TDIS parameters.

Appendix A

TDI - hBN blocks measurements and positions

In this appendix, numerical results obtained from the TDI - hBN blocks measurements are reported. Measurements setup and procedure were described in section 3.2. In Table A.1 only the measurable blocks are reported and each of them can be identified from its *serial number* (SN). Beside the SN, we have the TDI and the jaw they belong to, the measured sheet resistance (R_s) and the date in which the measurement was performed. The blocks positions in the respective jaws according to their SNs are reported in Table A.2.

SN	TDI	Jaw	R_s [$\Omega/\square$]	Measurement date
129	8	Bottom	$0.310 \pm 3\%$	15-Mar-16
152	8	Bottom	$0.626 \pm 7\%$	18-Mar-16
121	8	Bottom	$1.190 \pm 20\%$	18-Mar-16
113	8	Bottom	$0.469 \pm 5\%$	18-Mar-16
155	8	Bottom	$0.436 \pm 20\%$	18-Mar-16
146	8	Top	$0.773 \pm 8\%$	05-Apr-16
115	8	Top	$0.909 \pm 40\%$	05-Apr-16
109	8	Top	$1.190 \pm 0.7\%$	05-Apr-16
137	8	Top	$0.877 \pm 7\%$	05-Apr-16
110	8	Top	$1.070 \pm 4\%$	05-Apr-16
161	8	Top	$2.880 \pm 20\%$	05-Apr-16
112	8	Top	$1.670 \pm 20\%$	05-Apr-16
153	8	Top	$0.584 \pm 7\%$	05-Apr-16

Table A.1

SN	TDI	Jaw	R_c	Measurement date
138	8	Top	$0.649 \pm 4\%$	06-Apr-16
135	8	Top	$1.220 \pm 6\%$	06-Apr-16
141	2	Top	$0.488 \pm 6\%$	11-Apr-16
95	2	Top	$0.382 \pm 3\%$	11-Apr-16
91	2	Top	$0.545 \pm 7\%$	11-Apr-16
100	2	Top	$0.792 \pm 8\%$	11-Apr-16
92	2	Top	$0.294 \pm 0.9\%$	11-Apr-16
97	2	Top	$0.409 \pm 4\%$	11-Apr-16
94	2	Top	$0.256 \pm 1\%$	11-Apr-16
131	2	Top	$0.916 \pm 6\%$	11-Apr-16
85	2	Top	$0.318 \pm 3\%$	11-Apr-16
98	2	Top	$0.480 \pm 3\%$	11-Apr-16
128	2	Top	$0.686 \pm 1\%$	14-Apr-16
120	2	Top	$0.264 \pm 1\%$	14-Apr-16
106	2	Top	$0.433 \pm 2\%$	14-Apr-16
107	2	Top	$0.428 \pm 0.7\%$	14-Apr-16
126	2	Top	$0.516 \pm 5\%$	14-Apr-16
99	2	Top	$0.293 \pm 6\%$	14-Apr-16
96	2	Top	$0.319 \pm 1\%$	14-Apr-16
127	2	Bottom	$0.302 \pm 2\%$	18-Apr-16
88	2	Bottom	$0.448 \pm 1\%$	18-Apr-16
86	2	Bottom	$0.635 \pm 6\%$	18-Apr-16
125	2	Bottom	$0.465 \pm 6\%$	18-Apr-16
130	2	Bottom	$0.641 \pm 6\%$	18-Apr-16
87	2	Bottom	$0.328 \pm 2\%$	18-Apr-16
90	2	Bottom	$0.326 \pm 2\%$	18-Apr-16
104	2	Bottom	$0.646 \pm 2\%$	18-Apr-16
117	2	Bottom	$0.308 \pm 1\%$	18-Apr-16
116	2	Bottom	$0.284 \pm 9\%$	18-Apr-16
101	2	Bottom	$0.325 \pm 1\%$	19-Apr-16

Table A.1

SN	TDI	Jaw	R_c	Measurement date
124	2	Bottom	$0.645 \pm 3\%$	19-Apr-16
84	2	Bottom	$0.256 \pm 2\%$	19-Apr-16
105	2	Bottom	$0.307 \pm 0.8\%$	19-Apr-16
103	2	Bottom	$0.600 \pm 2\%$	19-Apr-16
102	2	Bottom	$0.638 \pm 2\%$	19-Apr-16
123	2	Bottom	$0.495 \pm 8\%$	19-Apr-16

Table A.1: TDIs blocks' measurement results for LHC run 2015.

	Serial Numbers			
	TDI2		TDI8	
Position	Top jaw	Bottom jaw	Top jaw	Bottom jaw
01	144	142	163	164
02	100	87	135	114
03	91	90	138	129
04	95	104	153	155
05	141	127	112	149
06	131	86	147	148
07	94	125	139	158
08	97	130	122	160
09	92	88	161	154
10	107	105	108	133
11	126	103	110	136
12	99	102	134	113
13	96	123	118	159
14	98	116	137	121
15	128	101	140	152
16	120	124	115	119
17	106	84	146	132
18	85	117	109	111

Table A.2: TDI blocks' positions with respect to the beam entrance for run 2015.

Appendix B

TDIS tune shift derived from CST simulations

In this appendix we reported the tune shift numerical results of all the simulations we performed on the TDIS, for a single bunch with 9 cm bunchlength and N = 1.15×10^{11}. Despite TDIS will replace the TDI for HL-LHC project, the parameters used to calculate these values are the LHC's ones. The main comparisons and some plot derived from these data are presented in chapter 6.

newgap	Re[ΔQ_v]		
	no fingers	far fingers	close fingers
1 *mm*	2.19×10^{-5}	2.19×10^{-5}	2.19×10^{-5}
5 *mm*	3.41×10^{-5}	3.38×10^{-5}	3.26×10^{-5}
10 *mm*	3.80×10^{-5}	3.77×10^{-5}	3.65×10^{-5}
15 *mm*	3.98×10^{-5}	3.96×10^{-5}	3.84×10^{-5}
20 *mm*	4.07×10^{-5}	4.05×10^{-5}	3.95×10^{-5}

Table B.1: Vertical tune shift for different newgap values with and without fingers at hgap = 3.8 mm. Absorber blocks are modeled with *Copper (annealed)*, from CST library.

newgap	Re[ΔQ_v]		
	no fingers	far fingers	close fingers
1 *mm*	9.18×10^{-5}	9.18×10^{-5}	9.18×10^{-5}
5 *mm*	1.04×10^{-4}	1.03×10^{-4}	1.02×10^{-4}
10 *mm*	1.07×10^{-4}	1.07×10^{-4}	1.06×10^{-4}
15 *mm*	1.09×10^{-4}	1.09×10^{-4}	1.08×10^{-4}
20 *mm*	1.10×10^{-4}	1.10×10^{-4}	1.09×10^{-4}

Table B.2: Vertical tune shift for different newgap values with and without fingers at hgap = 3.8 mm. Absorber blocks are modeled with graphite (σ = 66666 S/m).

newgap	Re[ΔQ_v]		
	no fingers	far fingers	close fingers
1 *mm*	2.71×10^{-8}	2.71×10^{-8}	2.71×10^{-8}
5 *mm*	3.04×10^{-8}	3.02×10^{-8}	2.94×10^{-8}
10 *mm*	3.21×10^{-8}	3.19×10^{-8}	3.06×10^{-8}
15 *mm*	3.37×10^{-8}	3.34×10^{-8}	3.19×10^{-8}
20 *mm*	3.51×10^{-8}	3.48×10^{-8}	3.30×10^{-8}

Table B.3: Vertical tune shift for different newgap values with and without fingers at hgap = 55.0 mm. Absorber blocks are modeled with *Copper (annealed)*, from CST library.

newgap	Re[ΔQ_v]		
	no fingers	far fingers	close fingers
1 *mm*	2.92×10^{-8}	2.93×10^{-8}	2.92×10^{-8}
5 *mm*	3.25×10^{-8}	3.23×10^{-8}	3.15×10^{-8}
10 *mm*	3.43×10^{-8}	3.40×10^{-8}	3.28×10^{-8}
15 *mm*	3.59×10^{-8}	3.55×10^{-8}	3.40×10^{-8}
20 *mm*	3.72×10^{-8}	3.70×10^{-8}	3.52×10^{-8}

Table B.4: Vertical tune shift for different newgap values with and without fingers at hgap = 55.0 mm. Absorber blocks are modeled with graphite (σ = 66666 S/m).

Bibliography

[1] P. Collier, "Welcome to the Beams Department," Presented on the 25th April at the Welcome Meeting for new Arrivals, CERN site of Prevessin, FR, 2016.

[2] M. Benedikt, P. Collier, V. Mertens, J. Poole, and K. Schindl, *LHC Design Report*. Geneva: CERN, 2004.

[3] G. Rumolo and F. Zimmermann, "Practical user guide for HEADTAIL," Tech. Rep. SL-Note-2002-036-AP, CERN, Geneva, Nov 2002.

[4] C. Zannini, L. Rivkin, and G. Rumolo, *Electromagnetic Simulation of CERN accelerator Components and Experimental Applications*. PhD thesis, Ecole Polytechnique, Lausanne, Mar 2013. Presented 15 Apr 2013.

[5] N. Biancacci, L. Palumbo, M. Migliorati, E. Métral, and B. Salvant, *Improved techniques of impedance calculation and localization in particle accelerators*. PhD thesis, Rome U., Apr 2014. Presented 07 05 2014.

[6] N. Mounet, L. Rivkin, and E. Métral, *The LHC Transverse Coupled-Bunch Instability*. PhD thesis, Ecole Polytechnique, Lausanne, Mar 2012. Presented 2012.

[7] K. Wille, *The Physics of Particle Accelerators - An Introduction*. Great Clarendon Street, Oxford OX2 6DP: Oxford University Press, 2000.

[8] B. Holzer, "CAS lectures - Transverse Dynamics." `http://cas.web.cern.ch/cas/CzechRepublic2014/Lectures/Lectures.html`, 31-08-2014/12-09-2014.

[9] S. Y. Lee, *Accelerator physics; 3rd ed.* Singapore: World Scientific, 2012.

[10] A. Chao, *Physics of Collective Beam Instabilities in High Energy Accelerators*. Wiley Series in Beam Physics and Accelerator Technology, Wiley, 1993.

[11] F. J. Sacherer, "Transverse bunched-beam instabilities," Tech. Rep. CERN-PS-BR-76-21, CERN, Geneva, Nov 1976.

[12] W. Herr and F. Schmidt, "A MAD-X Primer," p. 32 p, Jun 2004.

[13] E. Métral, "JUAS lectures - Longitudinal Dynamics." `http://emetral.web.cern.ch/emetral/`, 11-01-2016/18-03-2016.

[14] N. Mounet, *ImpedanceWake2D User Manual*. CERN. `https://impedance.web.cern.ch/impedance/Codes/ImpedanceWake2D/user_manual_todate.txt`.

[15] S. Redaelli, "LPCC lectures." `indico.cern.ch`, 07/09-04-2010.

[16] E. Bonanno, N. Biancacci, F. Caspers, I. Lamas Garcia, B. Salvant, and W. Vollenberg, "TDIs Resistivity Measurements," Presented on 25/04/2016 at the Impedance Meeting, CERN site of Meyrin, 6-R-012, 2016.

[17] MATLAB, *version 8.6.0 (R2015b)*. Natick, Massachusetts: The MathWorks Inc., 2015.

[18] S. S. Cohen, G. S. Gildenblat, and N. G. Einspruch, *Metal semiconductor contacts and devices*. VLSI electronics microstructure science, New York, NY: Academic Press, 1986.

[19] N. Mounet and E. Métral, "Electromagnetic fields and beam coupling impedances in a multilayer flat chamber," Dec 2010.

[20] F. Roncarolo, F. Caspers, T. Kroyer, E. Métral, and B. Salvant, "Comparison between Laboratory Measurements, Simulations and Analytical Predictions of the Resistive Wall Transverse Beam Impedance at low frequencies," p. 4 p, Aug 2008.

[21] M. Sands and J. Rees, "A Bench Measurement of the Energy Loss of a Stored Beam to a Cavity," Tech. Rep. LBL-PEP-NOTE-95. PEP-95. SLAC-TN-2005-051, Lawrence Berkeley Nat. Lab., Berkeley, CA, Aug 1974.

[22] V. G. Vaccaro, "Coupling impedance measurements: an improved wire method," Tech. Rep. INFN-TC-94-023, INFN, Rome, Nov 1994.

[23] N. Biancacci, "TDI impedance update," Presented on the 25th February at the Impedance Meeting, Salle conference BE (CERN), 2016.

[24] M. Gasior and R. Jones, “High Sensitivity Tune Measurement by Direct Diode Detection,” p. 3 p, Apr 2005.

[25] E. Bonanno, N. Biancacci, and B. Salvant, “TDI - Tune Shift Measurements vs Simulations,” Presented on 26/05/2016 at the TDIS Meeting, CERN site of Prevessin, 864/2-D17, 2016.

[26] E. Bonanno, N. Biancacci, J. Muller, and B. Salvant, “TDI - Updates on Tune Shifts and Phase Measurements,” Presented on 09/05/16 at the 78th HSC Section Meeting, CERN site of Meyrin, 6-R-012, 2016.

[27] CST, “Computer Simulation Technology.” `https://www.cst.com/`, 2015–2016.

[28] H. Henke and W. Bruns, “Calculation of Wake Potentials in General 3D Structures,” p. 3 p, 2006.

[29] W. Panofsky and W. Wenzel, “Some considerations concerning the transverse deflection of charged particles in radio-frequency fields,” *Rev. Sci. Instrum.*, vol. 27, p. 967, 1956.

[30] T. Weiland and R. Wanzenberg, “Wake fields and impedances,” *Lect. Notes Phys.*, vol. 400, pp. 39–79. 54 p, May 1991.

[31] E. Bonanno, D. Amorim, N. Biancacci, and B. Salvant, “TDIS - Simulations,” Presented on 28/07/2016 at the 2nd Impedance Working Group Meeting, CERN site of Meyrin, 6-R-012, 2016.

[32] L. Rossi and O. Brüning, “High Luminosity Large Hadron Collider A description for the European Strategy Preparatory Group,” Tech. Rep. CERN-ATS-2012-236, CERN, Geneva, Aug 2012.

[33] J. Uythoven, N. Biancacci, C. Bracco, O. Frasciello, L. Gentini, B. Goddard, A. Lechner, F. Maciariello, A. Perillo Marcone, B. Salvant, N. V. Shetty, G. Steele, F. Velotti, and M. Zobov, “Injection Protection Upgrade for the HL-LHC,” no. IPAC-2015-TUPTY051, p. TUPTY051. 4 p, 2015.

[34] CERN, “High Performing Computing.” `https://twiki.cern.ch/twiki/bin/viewauth/PESgroup/HpcCSTBatch/` only available with CERN credentials. Responsible: Michal Husejko (CERN).

[35] E. Bonanno and M. Husejko, “HPC for CST simulations,” Presented on 25/07/2016 at the Impedance Meeting, CERN site of Meyrin, 6-R-012, 2016.

List of Figures

List of Tables